aerospace

MDPI

Article

Design and Ground Simulation Performance Test of Coring Sampler for Mars Drilling and Sampling

Wei Xu [1], Yuyang Liu [1], Jie Ji [2], Ye Tian [1,*], Yachen Sun [3], Wenhui Guo [4], Jiahang Zhang [1], Weilong Wang [1], Jialin Zhang [5], Weiwei Zhang [3,*] and Yafang Liu [2]

[1] School of Light Industry, Harbin University of Commerce, Harbin 150028, China; hljhrbxw@163.com (W.X.)
[2] Institute of Spacecraft System Engineering, Beijing 100094, China
[3] State Key Laboratory of Robotics and Systems, Harbin Institute of Technology, Harbin 150028, China
[4] Guizhou Aerospace Qunjian Precision Machinery Co., Ltd., Zunyi 563099, China
[5] Faculty of Engineering, The University of Sydney, Sydney 2006, Australia
* Correspondence: tian8154@126.com (Y.T.); zweier@hit.edu.cn (W.Z.)

Abstract

The complex composition and extremely harsh, uncertain surface conditions on Mars impose stringent requirements on the coring performance and fault tolerance of a coring sampler. To satisfy the drilling and coring requirements of Martian soil–rock composite strata, a coring sampler capable of multiple repeated sampling operations is designed, which enables reliable acquisition and preservation of core samples. Drilling and coring experiments are conducted on simulated Martian soil with different particle size distributions and relative densities, as well as basalt specimens. The coring efficiency of the developed bit for Martian soil and rock under diverse working conditions, together with its wear characteristics during repeated coring, is systematically investigated. The results indicate that the proposed coring sampler structure is well adaptable to Martian soil–rock composite drilling. The coring mass of simulated Martian soil increases with increasing advance-to-rotation ratio and relative density, as well as decreasing median particle size. The coring mass of specimens with 91.7% relative density is significantly higher than that of 72.8%, and the maximum single coring mass of fine-grained pure regolith specimens reaches 19.32 g. During basalt coring, higher rotational speeds lead to more severe bit wear and more pronounced temperature elevation, with a peak temperature of 372.4 °C at 120 r/min. A rotational speed of 110 r/min achieves the best compromise between core integrity and bit service life, exhibiting excellent long-term operational stability and favorable cutting–rock-breaking matching performance. The results of this research provide a reference scheme and data support for future Martian soil–rock composite coring and drilling exploration missions.

Keywords: simulated Martian regolith; basalt; coring sampler; drilling performance

Check for updates

Academic Editor: Paolo Tortora

Received: 13 May 2026
Revised: 31 May 2026
Accepted: 1 June 2026
Published: 4 June 2026

Copyright: © 2026 by the authors. Licensee MDPI, Basel, Switzerland. This article is an open access article distributed under the terms and conditions of the Creative Commons Attribution (CC BY) license.

1. Introduction

In future Mars exploration missions, analyzing pristine Martian geological materials to decipher planetary evolution, climatic variations, and potential bio-signatures is widely recognized as one of the primary scientific objectives [1,2]. Accordingly, core drilling and regolith sampling of the Martian surface and subsurface represent the most effective technical pathway for obtaining in situ Martian geological information. A stable and reliable automated sampling system is therefore a critical prerequisite for the successful

implementation of Martian geological sampling missions [3,4]. As the executive end-effector that directly interacts with complex and unknown Martian geological media and endures extreme drilling environments, the structural rationality and operational reliability of the coring sampler directly determine sampling efficiency, sample quality, and service life.

A wide range of drilling tools have been developed for deep-space exploration over the years. For the drilling tool equipped on the EADS Astrium rover in the first mission of ESA's Aurora Exploration Programme, the drill bit tip can retract into the drill rod to achieve state switching between the drilling and sampling phases [5]. This drill bit adopts a basic conical configuration, with four cutting edges uniformly distributed along its circumference, and cutting–crushing edges with self-guiding capability are arranged at the bit tip. Similarly, the Sampling, Drilling and Distribution (SD2) subsystem, equipped on the Philae lander employed by ESA for the exploration of Comet 67P/Churyumov-Gerasimenko, also features a drill bit with conical base configurations [6]. Supporting two operational modes (drilling and sampling), the SD2 drill bit is integrated with two polycrystalline diamond (PCD) cutting edges. It has an outer diameter of 12 mm and an inner diameter of 2.5 mm, with a practical maximum drilling depth of approximately 23 cm.

To prepare for the ExoMars program, Galileo Avionica (Milan, Italy) collaborated with Helsinki University of Technology to develop a Drill with Hammering Mechanism (DHM) [7]. The team also carried out comparative tests on commercial drill bits with different structures and proposed a novel thin-walled coring bit. Experimental results show that this coring bit exhibits excellent drilling and coring efficiency in granite under the following operating parameters: rotational speed of 0.26 r/min, penetration rate of 0.022 mm/min, impact frequency of 1–2 Hz, and a thrust of 100 N.

NASA's Jet Propulsion Laboratory (JPL) designed a dedicated coring bit for the Mars Sample Return (MSR) mission. This drill bit adopts a flat-body configuration, with four cemented carbide cutting edges embedded on its end face. Radial chip removal grooves are machined on the rake face of the cutting edges, which are helically connected to the drill rod [8,9].

Honeybee Robotics (Longmont, CO, USA) developed a compact polycrystalline diamond compact (PDC) coring bit for hard extraterrestrial materials. Its cutting body is made of tungsten carbide alloy, and four helical convex inserts mounted with diamond-impregnated cutting segments are distributed on the annular surface. When drilling in ice-bearing regolith, frictional heat may melt local ice, which subsequently refreezes. The resulting icy debris accumulates between diamond grains and greatly impairs drilling efficiency [10].

The TE-C 3X drill bit, developed by Hilti (Kaufering, Germany), is mainly used for percussive drilling tests on Martian and Lunar rock analogs.

It features a double-groove square-section helical structure with an axial pitch of 1/2 inch and an outer diameter of 3/4 inch. Four hemispherical structures at the bit end function as chip evacuation channels [11].

The drilling instrument aboard NASA's Curiosity rover comprises a cemented carbide shovel-type bit, a sample collection sleeve, and a sample chamber. Samples enter the collection sleeve through the deep grooves on both sides of the shovel-shaped bit, while a spiral conveying rod transports samples into the sample chamber. This drill bit exhibits wide adaptability to various drilling targets, from soft kaolinite to hard basalt [12].

In addition to conventional coring drills, compact penetrators have also been applied to planetary exploration. The failed European Beagle 2 lander and NASA's Mars InSight lander both carried a miniature drill-type penetrator named the "Mole" [7]. This device employs a direct-push drilling and sampling mechanism with a straight insertion tube, which converts

the potential energy stored in an internal compressed spring into kinetic energy to achieve forward penetration. The barbs, intended to increase the friction coefficient between the device and regolith, expand the effective cross-sectional area of the Mole and thereby hinder its penetration. Moreover, sand grains easily accumulate behind the barbs and restrict their retraction and folding. Combined with these design flaws and inadequate pre-launch testing, the HP3 InSight Mole ultimately failed to penetrate the Martian regolith to any appreciable depth [13,14].

Despite the rich experience accumulated from existing missions, Martian drilling faces far more severe challenges than conventional terrestrial drilling. The Martian surface presents a complex geological environment dominated by loose regolith, with discrete hard rock masses distributed locally, thereby exhibiting a typical regolith–rock composite stratigraphic characteristic [15]. Extensive alteration occurs across most of the Martian surface, and sedimentary rocks have even formed in some areas. This makes the mechanical properties of Martian surface soils and rocks highly complex and variable [16,17]. Among the hard lithologies likely to be encountered during Martian surface drilling operations, basalt represents one of the most prevalent rock types. For instance, surface rock exposures at the Viking 1 and Viking 2 landing sites are predominantly basalt, accounting for 6.9% and 17.6% of the surface coverage, respectively [18]. Drilling equipment is thus highly likely to encounter basalt formations at virtually any Mars landing site candidate. Accordingly, the ability to achieve effective drilling and sampling of basalt can be regarded as a fundamental mission requirement for Mars exploration.

The Rock Abrasion Tool (RAT) aboard the Spirit rover successfully abraded Martian basalt [19]. This instrument was designed to grind a circular region with a diameter of approximately 45 mm and a depth of several millimeters. The coring drill bit onboard NASA's Perseverance rover is specially developed for Martian rock formations and tasked with acquiring and caching rock core samples [20]. Although severe wear of the drill string occurred during the first drilling attempt, which brings great difficulties to repeated sampling at multiple locations across the Martian surface, the sampling system has operated reliably throughout the mission, with more than 20 rock cores collected and cached to date [21,22].

Evidently, minimizing the mass and complexity of drilling equipment necessitates an optimal strategy: adopting a unified drilling system with a single type of coring bit capable of penetrating most target formations.

Accordingly, the development of high-performance coring bits adaptable to the extreme Martian environment and capable of both regolith sampling and rock drilling has become an urgent requirement for Mars exploration sampling missions. Once deployed on Mars, drilling tools cannot be readily replaced or repaired in situ. Thus, their entire service life from the initial state to complete failure must be fully characterized and predicted during the mission design phase. Consequently, in-depth investigation of the wear mechanisms and characteristics of coring bits under Mars-simulated environmental and lithological conditions is critical to the design of robust sampling systems.

Cemented carbide, featuring high hardness, excellent wear resistance, and superior red hardness, is the preferred material for the cutting components of deep-space exploration drilling tools [19]. Targeting the specific demands of Mars exploration missions, this study focuses on the structural design and parameter optimization of a coring sampler, aiming to address the key challenges posed by complex Martian formations and high reliability requirements. Specifically, the work encompasses the structural design of the coring sampler, the determination of optimal operating parameters, and the analysis of its wear characteristics under Mars-simulated environmental conditions. This research is expected to provide reliable technical support for the engineering implementation of

Mars exploration drilling, laying a solid foundation for the long-term stable operation of sampling systems.

2. Scheme Design of Mars Coring Sampler

To date, no Martian regolith or rock samples have been returned to Earth. Knowledge of the mechanical properties of Martian regolith and rocks can only be derived and estimated via inverse analysis using in situ data from past Martian surface missions. Existing Mars exploration missions reveal that Martian regolith exhibits considerable diversity, especially in cohesion and flowability; particle sizes may vary from extremely fine to coarse, with flowability ranging from high to low [14]. The Martian surface encompasses a wide variety of rock structures, indicating that rock strength also presents substantial heterogeneity [23,24].

To satisfy the drilling and coring requirements for Martian regolith and rocks, the Martian coring sampler must be capable of coring operations across diverse regolith and rock types, while enabling reliable containment of acquired samples. Given the diversity and unpredictability of Martian regolith and rocks, a reusable coring sampler can significantly improve the fault tolerance of sampling operations. To minimize the weight and complexity of the coring sampler, adopting a single drilling system and a universal drill bit for all regolith and rock types represents the optimal strategy.

In response to the aforementioned design specifications, a novel coring sampler is proposed in this study. The coring sampler comprises a motor, a reducer, a bidirectional lead screw, sealing cantilever springs and a drilling tool, as illustrated in Figure 1a. The drilling tool is structurally divided into a pilot drill bit and a coring drill bit, which undertake the tasks of penetration drilling and core sampling respectively. Driven by the built-in motor inside the drill rod, the pilot drill bit can realize reciprocating linear motion along the axial direction. The upper and lower segments of the lead screw are designed with spiral grooves of opposite rotation directions, which enables reverse synchronous motion between the pilot drill bit and the sealing cantilever springs. A complete drilling and sampling cycle consists of five sequential working stages: full-face penetration, coring and sampling, sample orifice sealing, core retrieval, and sample ejection arrangement.

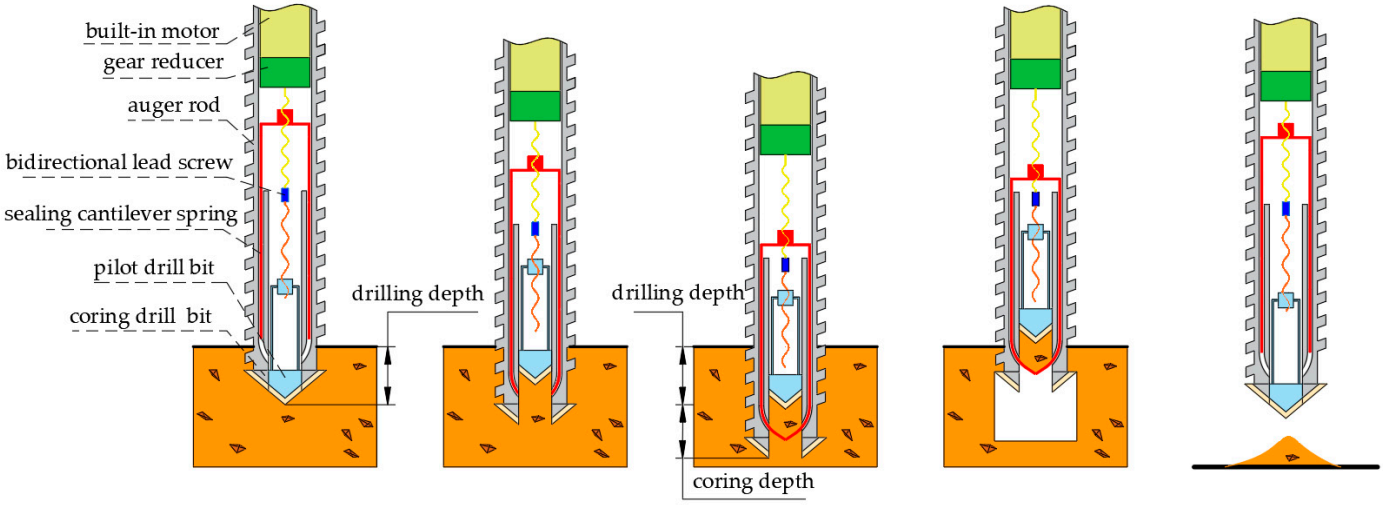


Figure 1. Mechanism and working process of the coring sampler.

(1) Full-face drilling. Prior to reaching the designated sampling depth, the drilling tool operates in full-face drilling mode. At this stage, the nut driving the pilot drill bit is

positioned at the forward-most working position of the bidirectional lead screw, with the pilot drill bit in the drilling state. Meanwhile, the nut for the sealing cantilever springs is located at the rearmost working position of the bidirectional lead screw, and the sealing cantilever springs remain on standby at the upper part of the drill rod cavity, as shown in Figure 1a.

(2) Core drilling. When the drill bit reaches the designated sampling depth, the motor is activated to drive the pilot drill bit to retract and move toward the core cavity via the bidirectional lead screw, switching the drilling tool to core sampling mode. Simultaneously, the sealing cantilever springs move downward under the drive of the bidirectional lead screw but do not extend into the core cavity. During this period, the coring mechanism continues to drill downward by a certain depth, allowing the sample to enter the core cavity and complete sample collection, as illustrated in Figure 1b.

(3) Sample orifice sealing. After sample collection is finished, the bidirectional lead screw drives the sealing cantilever spring to extend out from the side wall of the cavity and close beneath the samples. The collected regolith samples are thereby fully sealed inside the core chamber, completing the sample sealing process (Figure 1c).

(4) Core retrieval. Following sample sealing, the drilling tool is lifted to withdraw from the borehole. The core chamber remains fully sealed throughout the tripping process to ensure sample integrity, as displayed in Figure 1d.

(5) Sample ejection. Once the coring tool is moved to the sample ejection position, the sealing cantilever springs are driven upward by the bidirectional lead screw to open the core cavity. At the same time, the pilot drill bit moves downward to push the collected sample out of the core cavity. Subsequently, the drilling tool reverts core sampling mode to full-face drilling mode, ready for the next core sampling operation, as displayed in Figure 1e.

This proposed coring and sampling method can adapt to drilling and sampling operations of various types of soil and rock, enabling repeated sampling operations and effectively improving the efficiency and reliability of Mars surface sampling.

3. Design of Cemented Carbide Core Drill Bit for Mars Sampling

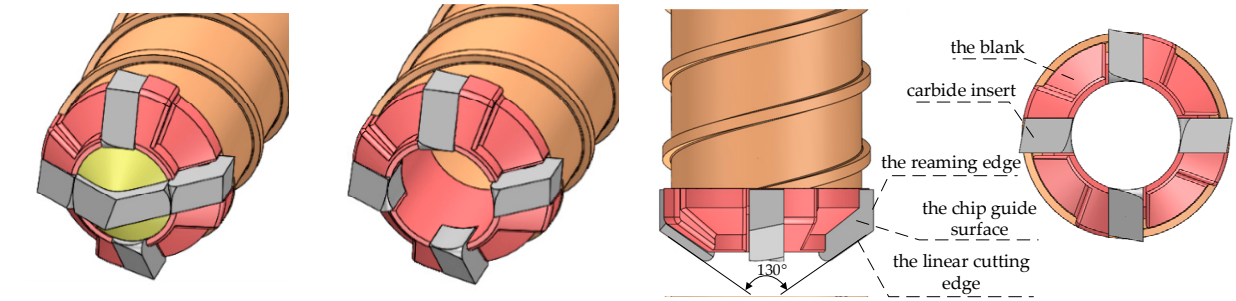
3.1. Design Overview

In light of the proposed sampling scheme and fundamental principles governing drilling tool design, this work also developed a cemented carbide drilling tool applicable to Martian soil–rock composite strata. The tool comprises a pilot drill bit and a core bit, and is configured with two distinct operational modes: full-face drilling and core drilling. During the full-face drilling mode, the pilot drill bit and core drill bit function synchronously to facilitate rapid penetration to the prescribed sampling depth, as illustrated in Figure 2a. Upon reaching the predetermined sampling depth, the pilot drill bit retracts, and the core bit independently performs coring operations, thereby switching the drilling tool to the core drilling mode, as shown in Figure 2b.

The performance of the core bit directly determines the success of coring operations. The core bit developed in this study consists of a conical body and four cemented carbide cutting blades circumferentially distributed at 90° intervals. The primary structure of the core bit is depicted in Figure 2c, and its key structural parameters are summarized in Table 1.

The conical body mainly serves to support the cutting blades and exert vertical force thereon. Its tapered geometry facilitates hole centering when drilling into rock. The linear cutting edges are responsible for cutting Martian soil and rock during penetration, enabling the core bit to advance smoothly into Martian soil and basalt, thus acting as the direct functional components for drilling and coring. Chip discharge channels are formed by the

blade surfaces in conjunction with the conical surface of the body, which efficiently convey cuttings of Martian soil and rock toward the rear end of the spiral groove in the drill rod.



(**a**) Full-face drilling mode (**b**) Core drilling mode (**c**) The coring drill bit structure

Figure 2. Two working modes of the drilling tool.

Table 1. Key structure parameters of core bit.

Structure Parameters	Value
Drill body form	Conical
Rake angle of cutting edge	0°
Clearance angle of cutting edge	15°
Number of cutting edges	4
Bottom protrusion height	2 mm
Outer protrusion height	2 mm

3.2. Design of Cemented Carbide Core Bit

3.2.1. Design of Bit Body

The selection of the cone angle of the bit body is mainly determined by the hardness of the drilling target. For drilling relatively hard materials, a larger cone angle should be adopted from the perspective of drilling tool strength, whereas a smaller cone angle is suitable for softer materials. The Mohs hardness of medium carbon steel is approximately 5–6, and a cone angle of 125°–130° is recommended for drilling [25]. A larger cone angle of the body results in a smaller radial component of the drilling force during drilling, leading to higher drilling efficiency and better drilling stability. The hardest component in Martian soil is basalt, with a Mohs hardness of approximately 6 [26]. Considering comprehensively the hardness of the drilling target, drilling efficiency, and drilling stability, a cone angle of 130° was ultimately selected for the bit body.

3.2.2. Selection of Bit Bottom Protrusion and Outer Protrusion

The bottom protrusion and outer protrusion of the bit are shown in Figure 3, where v is the bit feed rate, n is the bit rotational speed, h_1 denotes the bottom protrusion height, and h_2 denotes the outer protrusion height. The bottom protrusion (h_1) is generally designed to be larger than the cutting depth per cutting edge (h_p), and is mainly affected by the expansion coefficient of the drilled medium (K_p), median particle size (D_p), bit rotational speed (n), feed rate (v), and the number of cutting edges (N). The outer protrusion (h_2) is mainly determined by the median particle size (D_p) of the drilled medium, and is generally set to 3–5 times D_p. The bottom protrusion (h_1) and outer protrusion (h_2) can be determined according to the following equations [21]:

$$h_1 > h_p = \frac{v}{n \cdot N} \cdot K_p \quad (1)$$

$$h_2 = (3 \sim 5) \cdot D_p \quad (2)$$

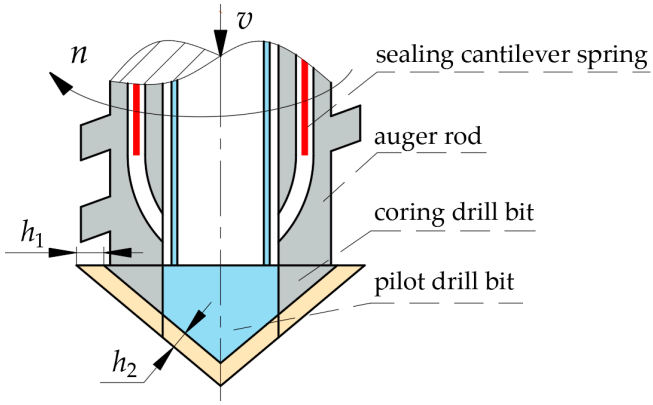


Figure 3. Schematic diagram of bottom protrusion and outer protrusion.

Considering the challenging working conditions characterized by low rotational speed and high feed rate, the experimental parameters were set as follows: rotational speed n = 100 r/min, feed rate v = 300 mm/min, expansion coefficient of simulated Martian rock K_p = 1.4, median particle size of simulated Martian rock D_p = 0.5 mm, and number of cutting edges N = 4. The value ranges of the bottom protrusion height h_1 and outer protrusion height h_2 were calculated accordingly $h_1 > h_p$ = 1.05 mm and h_2 = 1.5–2.5 mm, respectively. Finally, the bottom protrusion height h_1 was determined to be 2 mm, and the outer protrusion height h_2 was 2 mm.

4. Construction of the Drilling and Sampling Test Bench and Design of Drilling Tool Performance Tests

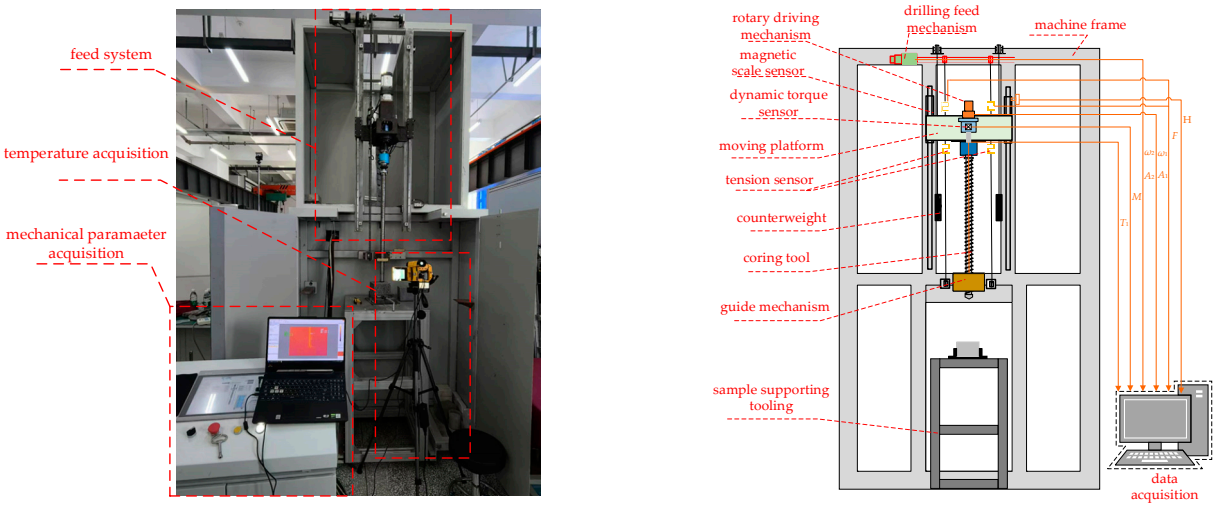
4.1. Composition of the Drilling and Sampling Test Platform

To investigate the sampling performance and drilling efficiency of the core bit under actual operating conditions, sampling tests on Martian soil and coring tests on basalt were conducted separately. All experiments were performed on a Martian regolith drilling test bench, which is mainly composed of a drilling feed system, a temperature acquisition system, and a mechanical property acquisition system, as depicted in Figure 4a. The drilling feed system enables the core bit to achieve rotational and feed movements, and is equipped with force, torque, and displacement sensors to acquire the mechanical responses during the drilling and sampling processes. The main structure of the drilling feed system is shown in Figure 4b. The key performance parameters of the Martian regolith drilling test bench are shown in Table 2.

Table 2. Key performance parameters of Martian regolith drilling test bench.

Name	Parameters
Drilling rig dimensions (length × width × height)	1350 mm × 1300 mm × 3200 mm
Driving rotational speed	0–500 r/min
Drive torque	0–30 N·m
Drilling rate	0–500 mm/min
Drilling force	0–1000 N
Maximum drilling depth	1200 mm

(1) Rotational drive of the drill. The drill has a rotational speed output range of 0–500 r/min and a torque output range of 0–30 N·m. The actual rotational speed of the drill is calculated by combining the measured value of the drive motor encoder with the reduction ratio. The torque of the drill is measured by a torque sensor installed in the rotational drive system.



(**a**) Physical test bench (**b**) Composition schematic of test bench

Figure 4. Martian regolith drilling test bench.

(2) Feed drive of the drill. The feed movement of the drill is realized by chain transmission, with a feed speed adjustment range of 0–500 mm/min and a feed force output range of 0–1000 N. The position and feed speed of the drill are measured by a magnetic grid ruler installed on the guide rail and the drive motor encoder, respectively. The feed force is obtained by subtracting the measured values of two tension sensors installed at the connection between the drill and the chain.

(3) Temperature measurement of the core bit. During the experiment, the temperature variation at the contact interface between the bit and basalt was measured and recorded in real time using a FLUKE TIX650 (Fluke Corporation, Everett, WA, USA) infrared thermal imager of the temperature acquisition system, whose temperature measurement range is −40–2000 °C, as illustrated in Figure 5. As drilling depth increases, the bit is gradually immersed into the basalt; at this stage, the temperature at the junction between the bit and the entrance of the basalt borehole is lower than the actual temperature of the bit. Therefore, to ensure the accuracy of temperature measurement, the bit was quickly lifted at the end of each drilling process, and its temperature variation was collected and recorded. The maximum measured temperature of the bit was used as the characteristic value to evaluate the temperature change in the bit during drilling.

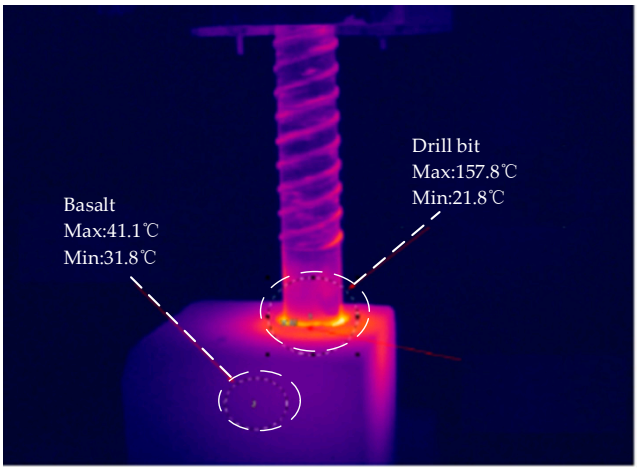


Figure 5. Schematic of drill bit temperature measurement.

(4) Morphology observation of bit cutting edges: After the drilling experiment, the macro- and micro-morphological characteristics of the bit cutting edge were obtained. A Nikon D7000 digital camera (Nikon, Tokyo, Japan) was used to capture macro-morphological characteristics, while a Sanqiang Taida coaxial optical electron microscope (Shenzhen, China) (Model: TD-LBTZG-4KH) was employed for micro-morphological characteristics, with a magnification range of 3.5–70 times. During the micro-morphological acquisition, the core bit was fixed on an adjustable-angle bench vice, and the vice angle was adjusted to position the bit cutting edge surface at the optimal imaging angle, as shown in Figure 6. The adjustable angle of the bench vice ranges from 0° to 90°, with a minimum adjustment angle of 1°, a jaw width of 100 mm, a jaw height of 45 mm, and a maximum opening of 105 mm.

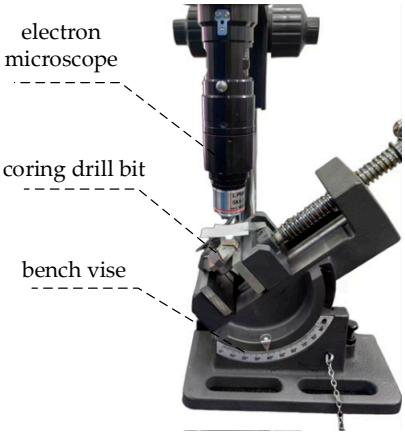


Figure 6. Schematic of cutting edge micro topography measurement.

4.2. Test Object

4.2.1. Core Drill Bit

Figure 7 shows the physical photograph of the core drill bit. The cutting edge is made of YG6X cemented carbide, which possesses high wear resistance and hardness, and its fine-grain microstructure enables the cutting edge to maintain sharpness for a long time, thereby prolonging the drill bit's service life. The substrate material is 40CrNiMoA, which has high strength and toughness, enabling it to withstand large torque and axial force generated during drilling and coring without plastic deformation or fracture.

It can also effectively alleviate vibration and impact during drilling, and its excellent fatigue strength further ensures the drill bit's service life. The cutting edges are directly embedded into the drill matrix and bonded via copper brazing, a connection method that provides high bonding strength and corrosion resistance to prevent the cutting edges from detaching during drilling and coring.

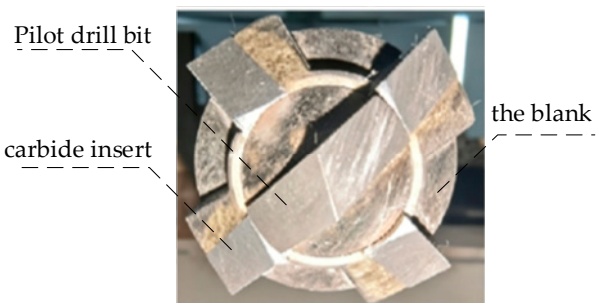


Figure 7. Physical prototype of drill bit.

4.2.2. Drilling Object

(1) Simulated Martian soil samples

The JLU-Mars series simulated Martian soil developed by Jilin University was adopted in the experiment [27]. The raw material was scoria collected from Shuangshan Volcano, Jingyu County, Jilin Province, China, and the simulated Martian soil was prepared through drying, mechanical crushing, particle size classification, and uniform mixing processes. Chemical compositions of scoria raw material are given in Table 3. The relative density of the simulated Martian soil samples was regulated using the three-dimensional vibration compaction method proposed by Chen Chongbin from Harbin Institute of Technology [28], which ensures uniform density distribution of the prepared simulated Martian soil samples.

Table 3. Chemical compositions of scoria raw material.

Na_2O	MgO	Al_2O_3	SiO_2	P_2O_5	SO_3	K_2O	CaO	TiO_2	MnO	FeO
4.07	4.83	17.03	48.69	0.43	0.03	2.57	6.48	2.19	0.09	12.14

At present, the typical proportion and content of rock particles in Martian soil remain unclear.

The typical proportion and content of rock particles in Martian regolith have not been well characterized. As the Curiosity rover traveled across the leeward sand accumulation zone at Rocknest; the dune material was disturbed by its left front wheel, and a large number of sand grains with particle sizes below 1 mm were observed on the resulting wheel ruts [29].

Therefore, several groups of rock particle ratios were designed in this study to investigate the sampling performance of the drilling tool under different working conditions. Five types of simulated Martian soil samples were prepared: fine-grained pure regolith, fine-grained mixed regolith, medium-grained pure regolith, medium-grained mixed regolith, and coarse-grained pure regolith. Specifically, the fine-grained pure regolith, medium-grained pure regolith, and coarse-grained pure regolith samples were all composed of particles smaller than 1 mm, with median particle sizes of 41 μm, 220 μm, and 690 μm, respectively, and they belonged to pure fine-grained pure regolith samples without any coarse particles. In contrast, the fine-grained mixed regolith and medium-grained mixed regolith samples were prepared by adding large particles (greater than 1 mm) with different sizes and proportions to the fine-grained pure regolith and medium-grained pure regolith samples, respectively. The particle size distribution of each sample is listed in Table 4, and the physical appearance of the samples is shown in Figure 8.

Table 4. Simulated Martian regolith particle size distribution.

Particle Size Class	Fine-Grained Pure Regolith	Fine-Grained Mixed Regolith	Medium-Grained Pure Regolith	Medium-Grained Mixed Regolith	Coarse-Grained Pure Regolith
Median particle size/μm	41	41	220	220	690
≤1 mm/%	100	60	100	75	100
1–2 mm/%	0	10	0	8	0
2–4 mm/%	0	8.5	0	5.5	0
4–10 mm/%	0	8.5	0	5.5	0
10–20 mm/%	0	5	0	2	0
20–30 mm/%	0	5	0	2	0
30–41 mm/%	0	3	0	2	0
≥42 mm	none	yes	none	yes	none
Total/%	100	100	100	100	100



(**a**) Pure fine sample



(**b**) Mixed sample with large particles

Figure 8. Physical appearance of simulated Martian regolith with different particle size gradations.

(2) Rock samples

Basalt, one of the most common and high-hardness rocks on Mars, was selected as the drilling object.

The basalt adopted in the experiment was dense basalt, whose chemical composition and macroscopic appearance were given in Table 5 and Figure 9 respectively. The basalt adopted in the experiment was dense basalt, as illustrated in Figure 9. The dimensions of the basalt sample were 13 cm × 15 cm × 15 cm (length × width × height), and the main mechanical properties are listed in Table 6.

Table 5. Chemical compositions of basalt.

Na_2O	Al_2O_3	SiO_2	K_2O	CaO	TiO_2	MnO	FeO
2.91	16.3	49.67	0.93	10.18	1.82	6.01	10.32



Figure 9. Basalt sample.

Table 6. Mechanical properties of basalt.

Performance Trait	Performance Parameters
Main mineral components	feldspar, pyroxene
Density	2.8–3.3 g/cm^3
Elastic modulus	2.1–21.1 GPa
Compressive strength	150–350 MPa
Shear strength	5–20 MPa
Mohs hardness	5–7

4.3. Test Design

In this study, decoupled tests were conducted to accurately compare and evaluate the drilling performance of the designed drill bit. By varying drilling parameters and drilling objects, these tests aimed to clarify the independent effects of working conditions and variables on drilling efficiency. The detailed experimental scheme is listed in Table 7.

Table 7. Drill bit drilling and coring test program.

Drilled Medium	Verifying Performance	Input Parameters	Output Parameters
Mars soil simulant	Drilling efficiency	Feed rate, Rotational speed, Particle size gradation, Soil density, Bit torque, Drilling depth	Drilling efficiency
	Coring mass	Advance-to-rotation ratio, Relative density, Sampling depth, Coring length, Particle gradation	Coring mass
Basalt sample	Drilling load	Feed rate, Rotational speed, Number of drilling runs, Drilling time	Drilling depth, Drilling force, Torque
	Bit wear resistance	Feed rate, Rotational speed, Number of drilling runs, Drilling time	Wear morphology, Flank wear width, Chip mass, Wear efficiency
	Bit temperature rise	Feed rate, Rotational speed, Number of drilling runs, Drilling time	Bit temperature

The experiment was carried out in constant feed rate mode at 1 mm/min. The bit rotational speeds were set to 100 r/min, 110 r/min, and 120 r/min, respectively. In total, 18 drilling tests were performed at each rotational speed, and each test was 10 min. During each test, drilling force, torque, depth, and bit temperature were recorded. After every six consecutive drilling tests (6th, 12th, and 18th tests), the macro- and micro-morphologies of cutting edges were observed, and the maximum flank wear width, bit mass loss, and chip mass were measured.

5. Tests and Analysis of Results

5.1. Results and Analysis of Drilling Experiments on Simulated Martian Soil Samples

5.1.1. Influence of Bit Advance-to-Rotation Ratio on Drilling Efficiency and Coring Mass

The purpose of these experiments is to investigate the influence of different speed–feed ratios on drilling efficiency and sampling mass. The speed–feed ratio is defined as the ratio of the drill bit rotational speed to the drill bit feed rate during drilling. In the experiment, the rotational speed was kept constant at 100 r/min, while the feed rate was set to 30 mm/min, 60 mm/min, and 90 mm/min, corresponding to speed–feed ratios of 100/30, 100/60, and 100/90. The experimental results regarding the effects of the speed–feed ratio on drilling efficiency and sampling mass are analyzed separately as follows.

(1) Analysis on the influence of penetration–rotation ratio on drilling efficiency in full-face drilling.

During drilling experiments on simulated Martian soil samples, the drill bit was operated in full-face drilling mode and fed into medium-grained simulated Martian soil specimens with a relative density of 72.8% at speed–feed ratios of 100/30, 100/60, and 100/90. The corresponding drilling depths were 80 mm, 300 mm, 700 mm, and 900 mm, aiming to investigate the influence of the speed–feed ratio on drilling efficiency under this working condition.

In this study, drilling power consumption was adopted to evaluate the drilling efficiency of the drill bit, and the effects of different speed–feed ratios were analyzed accordingly. The formula for evaluating drilling efficiency based on power consumption is given as follows:

$$\eta = \frac{W}{W + (k \times \rho)} \times 100\% \tag{3}$$

where η is the drilling efficiency (%), W is power consumption (W), k is soil density resistance coefficient (W·m^3/kg), and ρ is soil density (kg/m^3).

The density ρ of the medium particle size simulated Martian soil samples, is 1738 kg/m^3, and the soil density resistance coefficient k is 5.75 $\times$ 10^{-5} W·m^3/kg. Consequently, the product $k \times \rho$ remained constant, approximately 0.1 W. The expression for the drilling power consumption of the drill bit acting on the samples is presented as follows:

$$W = T \times \omega \tag{4}$$

In the formula, T is bit torque (N·m), and ω is rotational angular velocity (rad/s).

Figure 10 illustrates the relationship between the speed–feed ratio and drilling efficiency. Throughout the entire drilling process, the group with a speed–feed ratio of 100/30 achieved the highest drilling efficiency, with the maximum drilling efficiency reaching 3%. Specifically, the higher the speed–feed ratio, the higher the drilling efficiency, which also increased as the drilling depth increased.

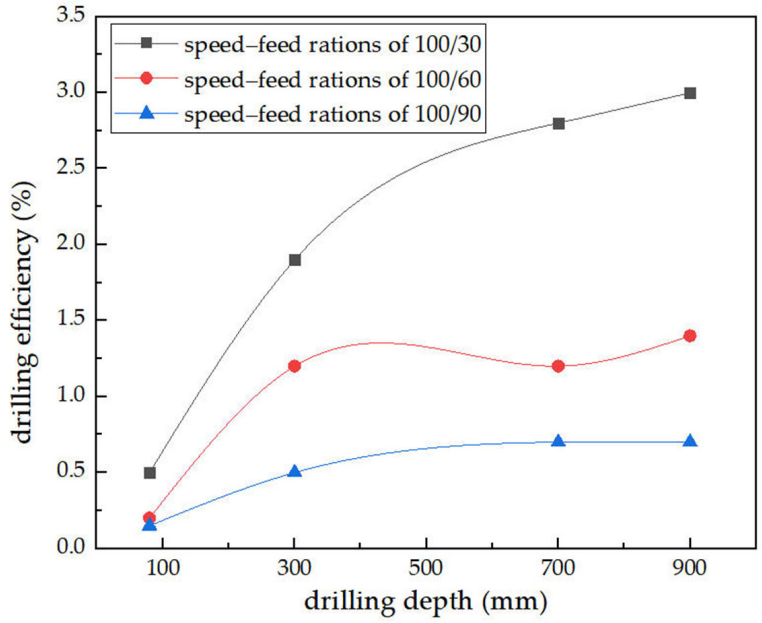


Figure 10. Drilling efficiency under different penetration-rotation ratios.

(2) Analysis of the influence of speed–feed ratio on sampling mass during coring drill.

After full-face drilling reached the predetermined depth, the pilot drill bit was retracted, and the drilling state was switched to the coring mode. Sampling drilling was then carried out downward to a depth of 60 mm under three rotational speed–feed ratio combinations (100/30, 100/60, 100/90). The sampling mass under each working condition was measured to reveal the influence of different speed–feed ratios on coring performance.

Figure 11 shows the variation law of sampling mass under various speed–feed ratios during coring drilling. It can be seen from the figure that the sampling mass presents a trend of first increasing and then decreasing with the rise in sampling depth. This variation is primarily dominated by the in situ confining pressure. At shallow sampling depths, the confining pressure is low and the constraint on simulated Martian soil is weak. The drill bit penetrates the formation easily, and the soil core enters the coring tube smoothly, contributing to a relatively high sampling mass. As the coring depth increases, the lateral confining pressure gradually rises, which markedly enhances the friction among the soil core, drill bit and inner wall of the coring cavity. Consequently, the soil core is prone to fragmentation and collapse, leading to a reduction in sampling mass. With further increase in coring depth, the continuous growth of confining pressure improves the overall integrity of the soil mass, suppresses core fragmentation and collapse, optimizes core forming stability, and thereby raises the sampling mass again.

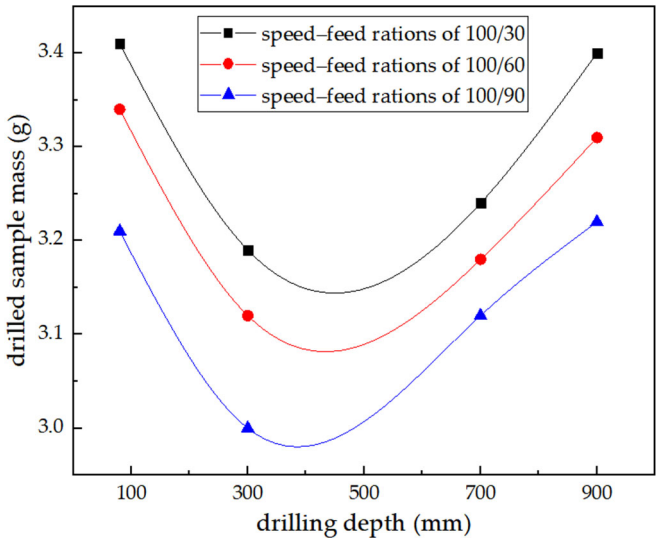


Figure 11. Influence of coring drilling parameters on sampling mass for medium-size particle samples.

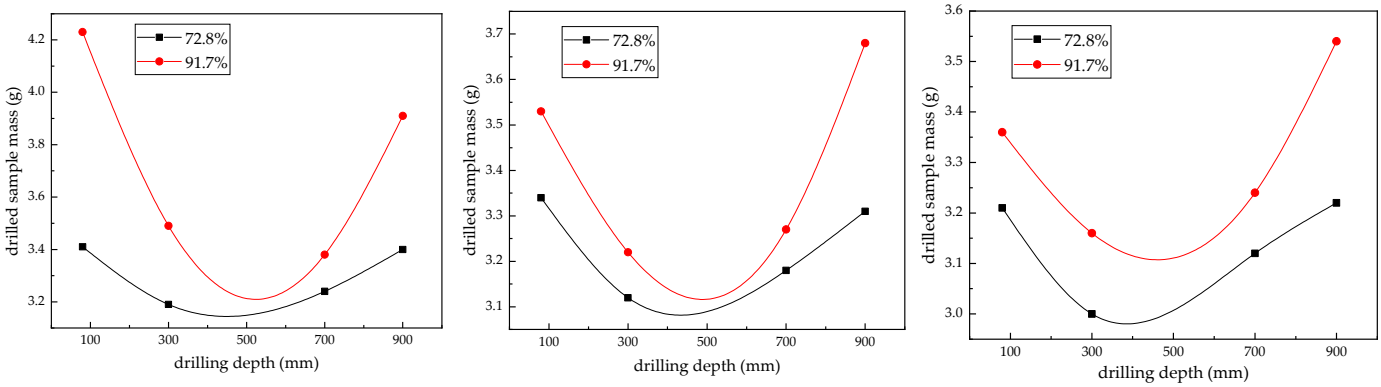
Additionally, the sampling mass increases with the rise in the speed–feed ratio during coring drilling. A higher speed–feed ratio enables a larger single cutting volume, weakening the disturbance and kneading action of the drill bit on the soil core. This maintains better soil core integrity and yields a higher sampling mass. By comparison, a lower speed–feed ratio aggravates repeated cutting and mechanical kneading, which easily induces core fragmentation and necking, and further reduces the sampling mass. Accordingly, for coring operations in simulated Martian regolith, appropriately lowering the rotational speed and adopting a higher speed–feed ratio can effectively mitigate soil disturbance, preserve soil core integrity, and improve the final sampling mass.

5.1.2. Influence of Relative Density on Coring Mass

Drilling experiments were carried out on simulated Martian soil specimens with identical particle size gradation but different compactness, so as to explore the influence of sample compactness on sampling mass. The tested medium-grained soil samples were

prepared at two relative densities of 91.7% and 72.8%. Four sampling depths (80 mm, 300 mm, 700 mm and 900 mm) and three speed–feed ratios (100/30, 100/60, 100/90) were adopted for coring tests, while the coring depth was fixed at 60 mm throughout the experiments.

Figure 12 presents the variation in sampling mass against sample relative compactness under the above test conditions. It can be seen that, with the same speed–feed ratio and drilling depth, specimens at a relative density of 91.7% always achieved a higher sampling mass than those at 72.8%. This reveals an obvious positive correlation between soil relative compactness and sampling mass: given identical drilling parameters, a higher relative compactness of simulated Martian soil corresponds to a greater sampling mass.



(**a**) speed–feed ratios of 100/30 (**b**) speed–feed ratios of 100/60 (**c**) speed–feed ratios of 100/90

Figure 12. Effect of relative density on sampling mass at different speed–feed ratios.

The physical mechanism behind this trend is as follows. Soil with higher relative compactness possesses a denser internal structure and better structural integrity. In the drilling and coring process, such soil can better resist deformation caused by cutting disturbance and extrusion effect, which suppresses the occurrence of core fragmentation, necking and collapse, and maintains favorable integrity and continuity of the soil core. Accordingly, higher relative compactness ultimately results in an increased sampling mass.

5.1.3. Influence of Particle Size Gradation on Coring Mass

Drilling tests were performed on simulated Martian soil samples with different particle size gradations to explore the effect of gradation characteristics on sampling mass. All test specimens were prepared at a fixed relative density of 72.8%, covering five categories: fine-grained mixed regolith, fine-grained pure regolith, medium-grained mixed regolith, medium-grained pure regolith, and coarse-grained pure regolith soil. Throughout the sampling process, the drill speed–feed ratio was set to 100/60, the sampling depth was fixed at 700 mm, and the coring length remained 60 mm.

Based on the above experimental conditions, Figure 13 compares the sampling mass of fine-grained pure regolith, medium-grained pure regolith and coarse-grained pure regolith specimens with median particle sizes below 1 mm. The results show that fine-grained pure regolith soil yields the highest average sampling mass of 19.32 g, followed by medium-grained pure regolith soil at 3.14 g, while coarse-grained pure regolith soil records the lowest value of 2.64 g. An evident trend can be concluded: the smaller the median particle size of simulated Martian soil, the greater the obtained sampling mass. This variation is mainly governed by particle-scale mechanical behavior. Soils with a smaller median particle size possess higher cohesion and stronger anti-disturbance capability, which effectively preserves soil core integrity and consequently increases sampling mass [30].

By contrast, soils with a larger median particle size exhibit greater flowability and weaker resistance to drilling disturbance, making the soil core more prone to fragmentation and collapse and thus reducing the final sampling mass.

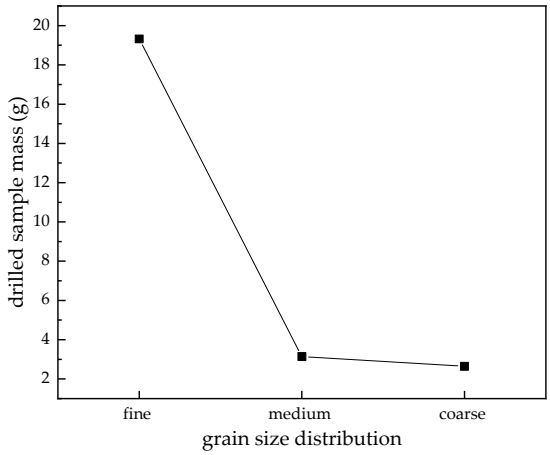


Figure 13. Comparison of sampling mass for samples with median particle size less than 1 mm.

On this basis, Figure 14 further compares the sampling mass of four graded specimens, namely fine-grained mixed regolith, fine-grained pure regolith, medium-grained pure regolith, and medium-grained mixed regolith soil, under identical drilling parameters. The results show that the sampling mass of the fine-grained mixed regolith specimen is 1.70 times that of the fine-grained pure regolith counterpart, and the value of the medium-grained mixed regolith specimen is 1.09 times that of the medium-grained pure regolith one.

It can be clearly concluded that the addition of particles larger than 1 mm effectively increases the sampling mass. The smaller the median particle size and the higher the soil cohesion, the more prominently large particles can enhance the sampling performance. The incorporation of oversized particles (>1 mm) creates a robust rigid skeleton within the soil matrix. This structure effectively boosts the mechanical strength and structural integrity of soil cores and mitigates core failure and collapse during coring operations. Meanwhile, finer-grained soils exhibit greater cohesion, which plays a positive role in maintaining core integrity. Such enhanced cohesion synergistically strengthens the skeleton effect of large particles, leading to a further improvement in overall sampling quality.

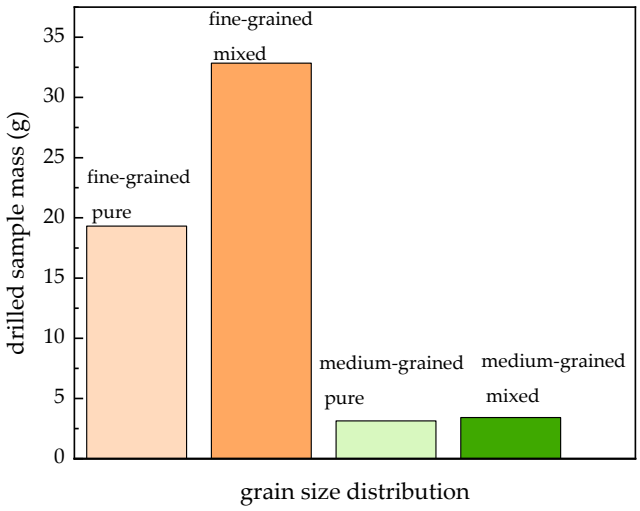
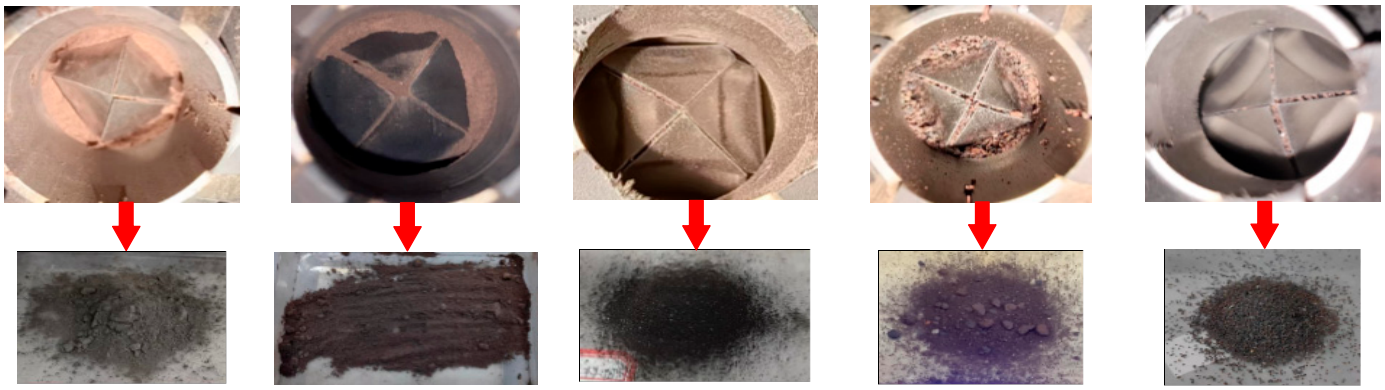


Figure 14. Effect of particles larger than 1 mm on sample sampling mass.

Figure 15 presents the spring-clip sampling and ejection status of the five simulated Martian soil specimens after coring drilling. It can be observed that the proposed sampling structure is capable of successfully completing the sampling and encapsulation process for specimens with various particle size gradations, demonstrating good adaptability to different graded soils.



(**a**) (**b**) (**c**) (**d**) (**e**)

Figure 15. Spring clip sampling and release state after coring. (**a**) fine-grained pure; (**b**) fine-grained mixed; (**c**) medium-grained pure; (**d**) medium-grained mixed; (**e**) coarse-grained pure.

Nevertheless, residual soil was found in the coring channel below the sealing structure for the fine-grained pure regolith, fine-grained mixed regolith, and medium-grained mixed regolith specimens, while no such residue was observed for the other two types. The underlying mechanisms of this phenomenon vary with particle gradation, and the specific analysis is as follows: For fine-grained pure regolith and fine-grained mixed regolith specimens, the soil exhibits low flowability and high cohesion; under the action of drilling force, high-strength soil agglomerates with force-chain self-locking are formed in the clearance between the spring clips and the coring chamber wall. These agglomerates failed to be fully dislodged during drill retrieval, which not only caused residual soil in the coring channel but also contributed to the significantly higher sampling mass of fine-grained pure regolith and fine-grained mixed regolith specimens compared with other types.

In contrast, since no residual soil was detected in the coring channel of the medium-grained pure regolith specimen, it can be inferred that the residual soil in the medium-grained mixed regolith specimen is not caused by force-chain self-locking, but by particle clogging. Specifically, during drill retrieval, large particles (>1 mm) in the medium-grained mixed regolith specimen entered the clearance between the spring clips and the coring chamber wall, where they interlocked and compressed with each other, eventually forming stable blockages that led to soil residue.

5.2. Drilling Test Results and Analysis of Basalt Samples

Rock sample drilling experiments were conducted in constant-speed feed mode at a feed rate of 1 mm/min. The drill bit rotational speed was set to 100 r/min, 110 r/min, and 120 r/min, respectively. Eighteen drilling runs were performed at each rotational speed, with each test lasting 10 min. Drilling force, torque, drilling depth, and bit temperature were recorded during each drilling run. After the 6th, 12th, and 18th runs, the macro- and micro-morphology of the cutting edges of the coring bit was examined, and the maximum flank wear width, total bit mass, and cutting mass were measured.

5.2.1. Analysis of Drilling Depth

Figure 16 shows the single drilling depth at the three rotational speeds. It can be seen that the drilling depth of the first run is the largest at each rotational speed, with values of 2.39 mm, 2.93 mm, and 3.54 mm at 100 r/min, 110 r/min, and 120 r/min, respectively. From the first to the fourth runs, the single drilling depth is largest at 120 r/min and smallest at 100 r/min. From the fifth to 12th runs, the single drilling depth becomes largest at 110 r/min and smallest at 120 r/min. During the 13th to 18th runs, the drilling depth at 120 r/min remains the smallest, while those at 100 r/min and 110 r/min are almost identical.

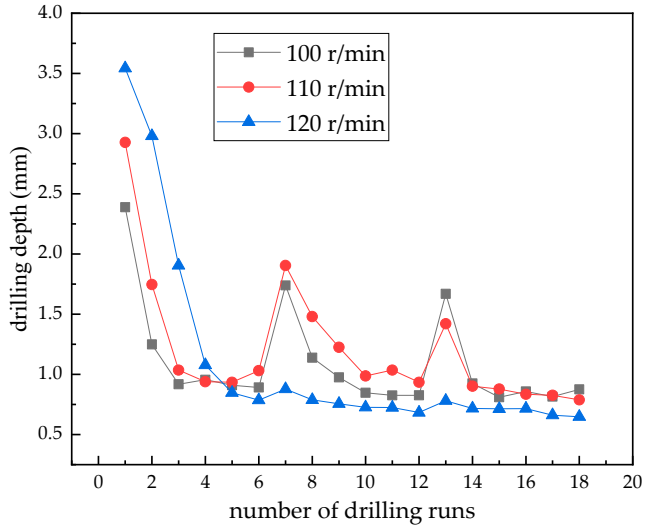


Figure 16. Comparison of single drilling depth at three rotational speeds.

Based on the above variation characteristics, it can be concluded that a higher rotational speed contributes to a larger single drilling depth in the initial drilling stage. Nevertheless, as drilling proceeds, gradual bit wear leads to a continuous reduction in single drilling depth. Among the three rotational speeds, the depth attenuation is the most pronounced at 120 r/min, while the attenuation rate is the slowest at 110 r/min. Notably, the drilling depths in the seventh and 13th runs are distinctly higher than those in adjacent runs, which is mainly attributed to the effect of basalt cuttings. Since the cuttings were collected and weighed after the sixth and 12th runs, no cutting accumulation existed between the cutting edges and the basalt sample during the seventh and 13th runs. It can therefore be concluded that residual basalt cuttings during drilling impede the drilling process and reduce the single drilling depth of the drill bit.

Figure 17 shows the cumulative drilling depth at the three rotational speeds. As illustrated, during the first to sixth runs, the total drilling depth reaches a maximum of 11.14 mm at 120 r/min, followed by 8.61 mm at 110 r/min, and a minimum of 7.31 mm at 100 r/min. From the seventh to 12th runs, the total drilling depths at 100 r/min, 110 r/min, and 120 r/min decrease by 13.13%, 12.17%, and 59.12%, respectively, relative to those in the first to sixth runs. During the 13th to 18th runs, the total drilling depths at 100 r/min and 110 r/min are similar, at 5.95 mm and 5.65 mm, whereas that at 120 r/min is the lowest at 4.24 mm. It can be observed that, with increasing bit wear, the total drilling depth over each six-run interval gradually decreases for all three speeds. The total depth declines most drastically at 120 r/min and most slowly at 110 r/min. For all 18 drilling runs, the cumulative drilling depth is the largest at 110 r/min (21.83 mm), followed by 120 r/min (19.93 mm), and the smallest at 100 r/min (19.61 mm).

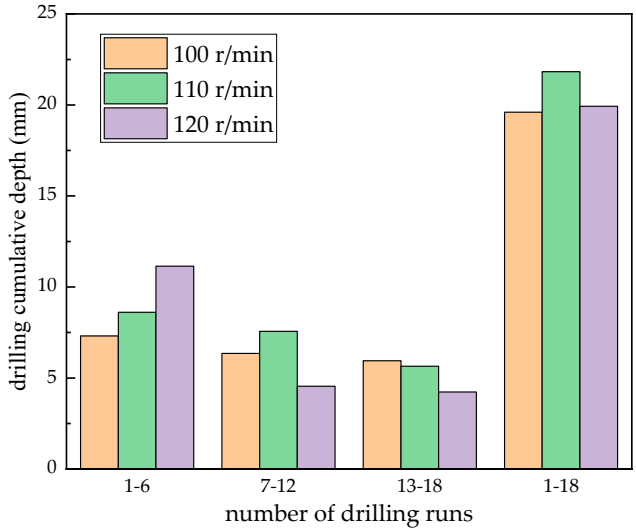
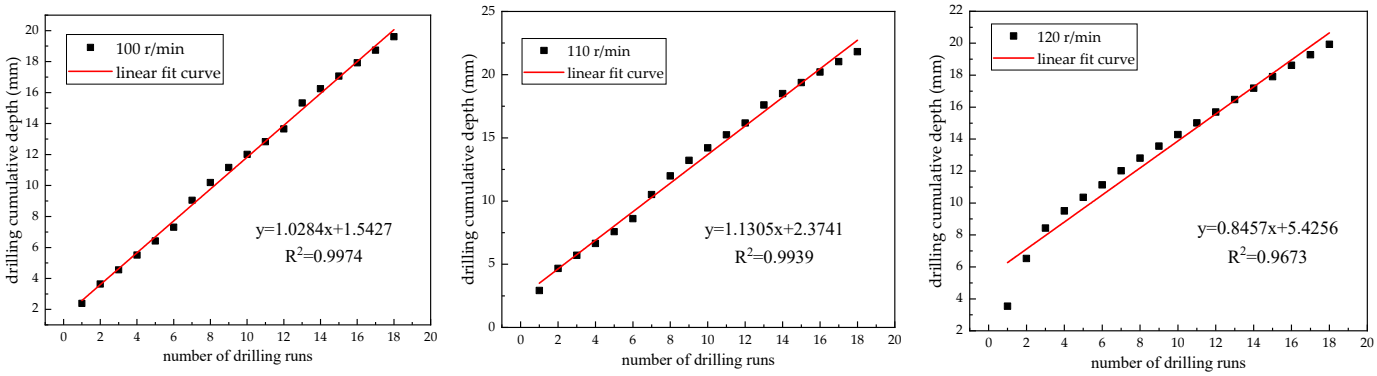


Figure 17. Comparison of cumulative drilling depth at three rotational speeds.

Further analysis shows that the cumulative drilling depth exhibits a linear positive correlation with the number of drilling runs at all three rotational speeds (100 r/min, 110 r/min, and 120 r/min), as depicted in Figure 18. The coefficients of determination R^2 of the linear fitting are 0.9974, 0.9939, and 0.9673, with corresponding slopes of 1.0284, 1.1305, and 0.8457, respectively. The slope at 110 r/min is the largest, indicating that the growth rate of the drilling depth with the number of runs is most significant at this rotational speed.



(**a**) 100 r/min (**b**) 110 r/min (**c**) 120 r/min

Figure 18. Linear regression between total drilling depth and number of drilling runs.

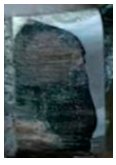
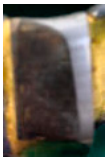
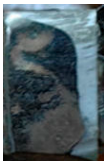
5.2.2. Analysis of Core Drill Bit Wear Resistance

This experiment aims to compare the bit wear behavior with increasing drilling runs under different rotational speeds, so as to reveal the evolution of drilling efficiency with progressive bit wear.

(1) Macroscopic morphology of flank wear.

Table 8 presents the macroscopic flank wear morphology of the drill bit after the sixth, 12th, and 18th drilling runs at the three rotational speeds. It can be seen that after the sixth run, the bit flank wear is slight, and the wear region on the flank face of individual cutting edges is barely distinguishable by visual inspection. After the 12th run, the wear area of the bit flank is significantly larger than that after the sixth run, and the wear zone on each cutting edge exhibits an approximately rectangular expansion. After the 18th run, the flank wear area further increases substantially.

Table 8. Table of macroscopic morphology of drill cutting edge wear at three rotational speeds.

Cutting Edge Number	Macroscopic Morphology of the Cutting Edge								
	100 r/min			110 r/min			120 r/min		
	6th	12th	18th	6th	12th	18th	6th	12th	18th
No. 1									
No. 2									
No. 3									
No. 4									

Further comprehensive comparison of the flank wear areas at the three rotational speeds across the three drilling stages indicates that the wear morphology of a single cutting edge maintains good self-similarity throughout the whole wear process. At 100 r/min and 110 r/min, the flank wear profiles present relatively regular rectangular shapes; in contrast, the wear morphology at 120 r/min develops into an irregular rectangular or approximate trapezoidal profile along the cutting edge. In terms of wear severity, 120 r/min yields the most serious wear, followed by 110 r/min, while 100 r/min produces the mildest flank wear.

Based on the above morphological comparison, it can be concluded that under the same number of drilling runs, higher rotational speed aggravates the flank wear of the core drill bit. At lower rotational speeds, the flank wear area propagates relatively uniformly, whereas with increasing speed, the wear evolution exhibits greater randomness and non-uniformity. This is mainly attributed to the high hardness of the experimental basalt, such that abrasive wear dominates the drilling process. A higher rotational speed gives rise to a higher cutting frequency and more frequent friction between the bit flank and basalt, resulting in more severe bit wear. Basalt contains internal pores with varying sizes and non-uniform distribution, causing inconsistent frictional resistance acting on the drill bit during drilling. Furthermore, the high hardness and poor drill ability of basalt induce radial runout during bit rotation, further leading to non-uniform loading and friction among different cutting edges. Such non-uniformity becomes increasingly pronounced with increasing rotational speed.

(2) Flank wear of core drill bit.

In this study, the average maximum flank wear width measured across the four cutting edges was taken as the evaluation index to characterize the overall flank wear degree of

the drill bit. The corresponding measurement method for maximum flank wear width is schematically shown in Figure 19.

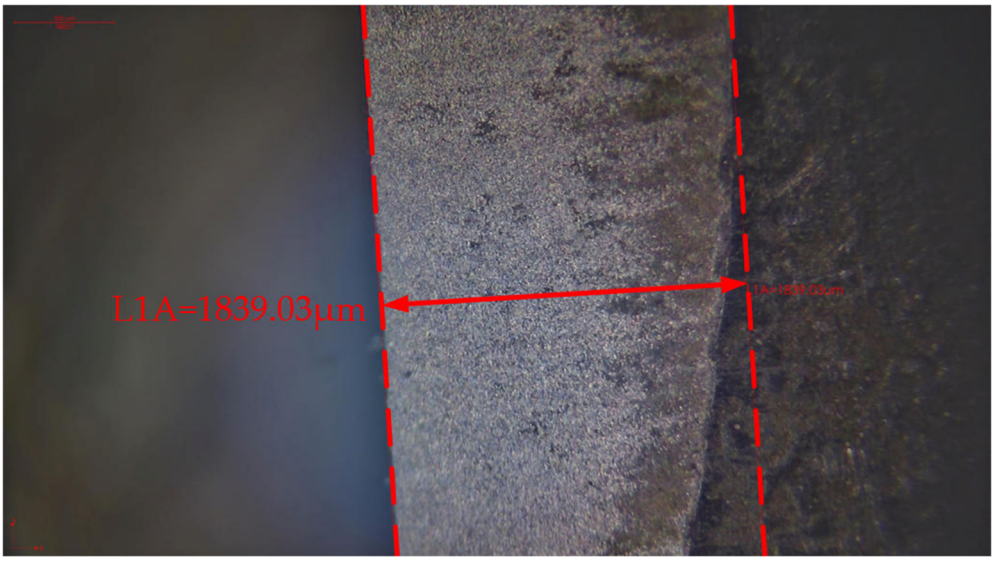
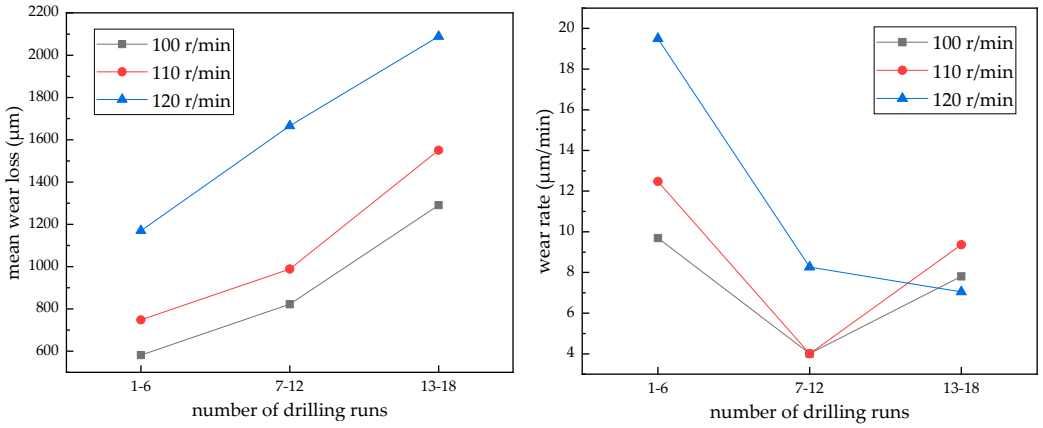


Figure 19. Measurement of maximum flank wear width of core drill bit.

On this basis, Figure 20 illustrates the variations in flank wear magnitude and wear rate with the number of drilling runs under the three rotational speeds.



(**a**) Wear amount variation (**b**) Wear rate variation

Figure 20. Wear characteristics of core drill bit flank.

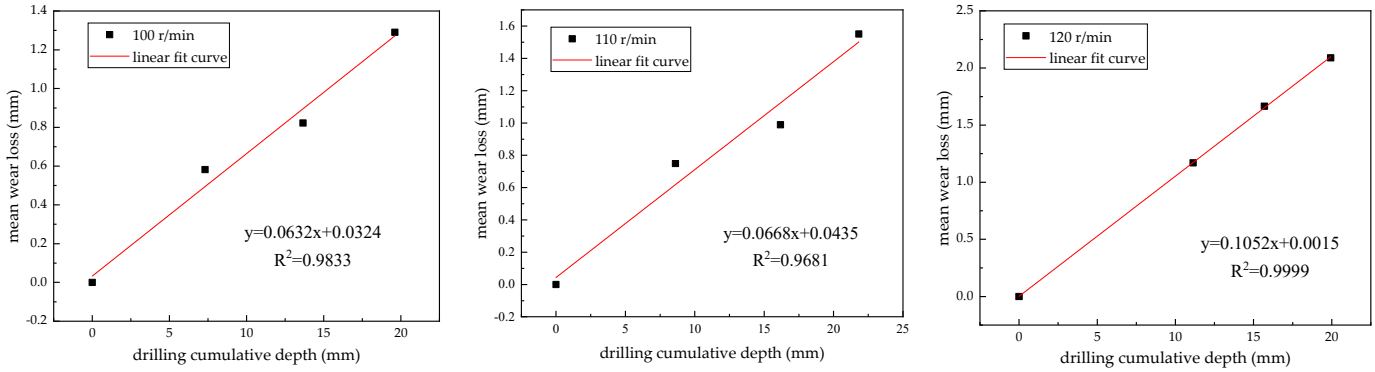
As shown in Figure 20a, the flank wear magnitude increases gradually after the 6th, 12th, and 18th drilling runs. The flank wear magnitude is the largest at 120 r/min, followed by 110 r/min, and the smallest at 100 r/min. After the 18th run, the flank wear magnitudes increase by 0.79, 1.07, and 1.22 times compared with those after the sixth run at 100 r/min, 110 r/min, and 120 r/min, respectively.

Figure 20b further presents the changing law of flank wear rate in different drilling stages. In the 1st–6th runs, the wear rates reach 9.70 μm/min, 12.47 μm/min and 19.50 μm/min at 100 r/min, 110 r/min and 120 r/min, respectively. In the subsequent 7th–12th runs, the wear rates drop to 0.41, 0.32 and 0.42 times their respective values in the first stage. During the 13th–18th runs, the wear rates rise again to 1.94, 2.34 and 0.85 times those recorded in the 7th–12th runs.

Combining the above results, the flank wear magnitude generally grows steadily with increasing drilling runs, and a higher rotational speed consistently aggravates flank

wear. In contrast, the evolutionary trend of wear rate differs distinctly among the three speeds: at 100 r/min and 110 r/min, the wear rate follows a decrease-then-increase pattern throughout the drilling process, while the wear rate at 120 r/min declines monotonically in the whole test period.

To further quantify this relationship, Figure 21 presents the linear regression between flank wear magnitude and cumulative drilling depth after the 6th, 12th, and 18th drilling passes. The results reveal that flank wear magnitude exhibits a strong positive linear correlation with cumulative drilling depth at all three rotational speeds, with coefficients of determination R^2 calculated as 0.9833, 0.9681 and 0.9999, respectively. The linear regression slope peaks at 0.1052 for 120 r/min, while the slopes for 100 r/min and 110 r/min are comparatively close, at 0.0632 and 0.0668 accordingly.



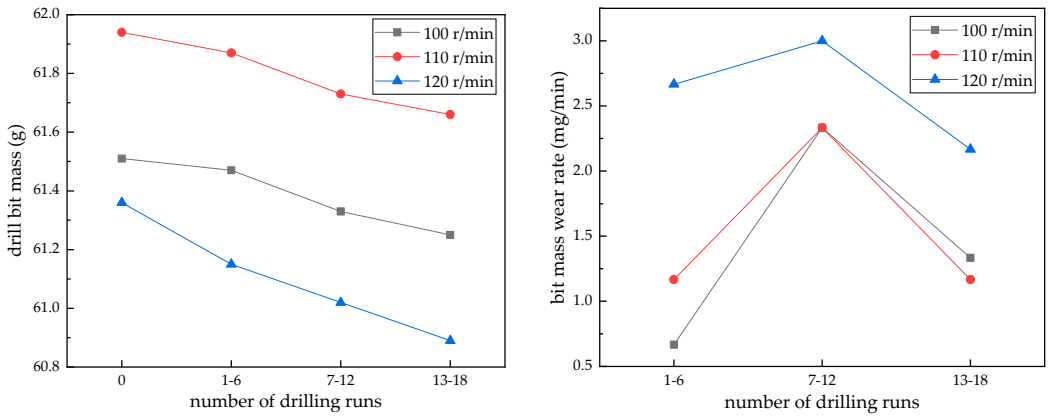
(**a**) 100 r/min (**b**) 110 r/min (**c**) 120 r/min

Figure 21. Linear regression relationship between flank wear of core drill bit and cumulative drilling depth.

Consistent with the regression results, as the cumulative drilling depth increases, the development of flank wear proceeds most rapidly at 120 r/min. By comparison, the wear growth rates at 100 r/min and 110 r/min are relatively slow and remain at a similar level.

(3) Mass loss of core drill bit.

Figure 22 shows the variations in bit mass loss and mass wear rate with increasing number of drilling runs.



(**a**) Variation in drill bit mass (**b**) Variation in mass wear rate

Figure 22. Variation in mass loss for core drill bit.

As shown in Figure 22a, the initial masses of the drill bits before drilling were 61.51 g, 61.94 g, and 61.36 g at 100 r/min, 110 r/min, and 120 r/min, respectively. After the third

drilling run, the drill bit at 120 r/min exhibited the greatest mass loss of 0.47 g. The mass losses for the bits at 100 r/min and 110 r/min were similar, at 0.26 g and 0.28 g, respectively.

It can be observed that the total mass of the drill bits gradually decreases with increasing drilling runs owing to progressive wear. The mass loss is largest at 120 r/min, whereas those at 100 r/min and 110 r/min are comparable.

Further inspection of Figure 22b reveals the evolution of mass wear rate in different drilling stages. From the first to the sixth drilling runs, the mass wear rate of the drill bit rises with increasing rotational speed, reaching 0.67 mg/min, 1.17 mg/min, and 2.67 mg/min at 100 r/min, 110 r/min, and 120 r/min, respectively. In the subsequent seventh to 12th runs, the mass wear rates at all three speeds are higher than those in the first to sixth runs. The rate reaches a maximum of 3.00 mg/min at 120 r/min, while the rates at 100 r/min and 110 r/min are identical at 2.33 mg/min. From the 13th to 18th runs, the mass wear rates at all three speeds decrease compared with those in the seventh to 12th runs. The rate remains highest at 120 r/min (3.00 mg/min), followed by 100 r/min (1.33 mg/min), and lowest at 110 r/min (1.17 mg/min).

Synthesizing the above results, the mass wear rate of the drill bit first increases and then decreases with an increasing number of drilling runs. The mass wear rate is highest at 120 r/min, while those at 100 r/min and 110 r/min are relatively comparable.

Notably, the evolutionary trends of bit flank wear morphology under the three rotational speeds are well consistent with the variations in flank wear magnitude and cumulative mass loss. This consistency further demonstrates that the drill bit delivers the poorest durability when drilling basalt at 120 r/min, while adopting 100 r/min and 110 r/min can achieve relatively better wear resistance and service durability.

(4) Drilling cuttings mass.

The morphology of basalt drilling cuttings generated at various rotational speeds is presented in Table 9. Basalt cuttings produced under all tested rotational speeds are uniformly fine-grained pure regolith powder, with no conspicuous large basalt particles observed. The basalt fine powder possesses high cohesiveness and forms force-chain self-locked agglomerates with diverse sizes and morphologies under natural accumulation. Since all basalt cuttings exist as fine powder, it can be inferred that the interaction between the drill bit and basalt is dominated by compressive grinding. Basalt is detached in the form of fine particles under the shearing, frictional and rolling actions of the drill bit.

On this basis, Figure 23 further characterizes the variation in basalt cutting mass throughout the whole drilling process. During the first to sixth drilling runs, a higher rotational speed generates a greater mass of cuttings. The cutting mass reaches the maximum value of 13.9 g at 120 r/min, followed by 11.84 g at 110 r/min, and the minimum value of 9.31 g at 100 r/min. The mass of basalt cuttings decreases gradually with an increase in drilling runs. From the seventh to 12th runs, the cutting masses at 100, 110 and 120 r/min decrease by 39.63%, 48.90% and 69.71%, respectively, compared with those in the first to sixth runs. From the 13th to 18th runs, the cutting masses further decrease by 26.16%, 29.42% and 22.80%, respectively, relative to those in the seventh to 12th runs. Over the entire first to 18th drilling runs, the total mass of cuttings is the largest at 110 r/min (22.16 g), followed by 120 r/min (21.36 g), and the smallest at 100 r/min (19.08 g). According to the above variation law of cutting mass, the cutting generation behavior matches the drilling performance best at 110 r/min, corresponding to the optimal comprehensive drilling efficiency.

Table 9. Table of basalt drilling chip morphology.

Rotational Speed (r/min)	Number of Drilling Runs		
	6th	12th	18th
100			
110			
120			

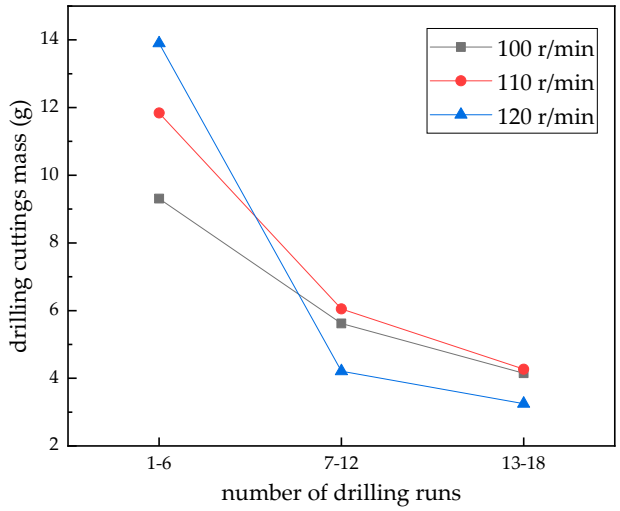


Figure 23. Mass variation in basalt drill cuttings.

(5) Wear efficiency ratio.

The wear efficiency ratio is defined as the ratio of the mass of drilling cuttings generated during drilling to the mass loss of the drill bit. A higher wear efficiency ratio indicates better durability and higher drilling efficiency of the drill bit.

As illustrated in Figure 24, the variation in the wear efficiency ratio with drilling runs and rotational speeds exhibits distinct stage characteristics. During the first to sixth drilling runs, the wear efficiency ratio decreases with increasing rotational speed. The ratio reaches the maximum value of 232.75 at 100 r/min, followed by 169.14 at 110 r/min, and the minimum value of 86.88 at 120 r/min. In the sixth to 12th runs, the wear efficiency ratios at all three speeds are lower than those in the first to sixth runs. The ratio at 120 r/min remains the smallest (12.38), while those at 100 r/min and 110 r/min are close, at 31.22 and 28.81,

respectively. During the 13th to 18th runs, the wear efficiency ratios further decreased. The ratio at 120 r/min is still the lowest (6.91), and the values at 100 r/min and 110 r/min are almost identical, at 15.96 and 15.25, respectively.

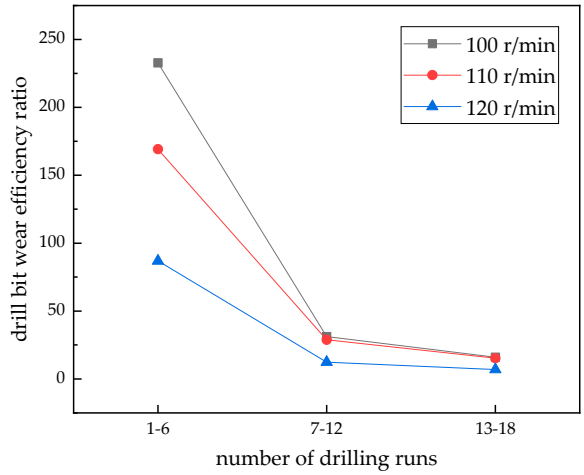


Figure 24. Wear efficiency ratio of core drill bit.

Synthesizing the above variation characteristics, it can be concluded that a higher rotational speed corresponds to a lower wear efficiency ratio, indicating poorer drill bit durability. Meanwhile, as the number of drilling runs increases, the wear efficiency ratio gradually decreases, implying a gradual degradation in drill bit durability. Overall, the drill bit exhibits the worst durability at 120 r/min, while the durability at 100 r/min and 110 r/min is similar, which is consistent with the previously observed wear and drilling performance trend.

(6) Core integrity.

Figure 25 displays the intact state of rock cores obtained during coring under different rotational speeds. At 100 r/min, the core fractured at the 12th drilling run, with a core length of 11.92 mm. At 110 r/min, fracture emerged at the 15th run, yielding a core length of 17.66 mm. In contrast, at 120 r/min, no core fracture appeared throughout all 18 drilling runs, and the core length reached 19.93 mm. It is evident that a higher rotational speed contributes to a more intact core and a higher core recovery ratio.



(**a**) 100 r/min (**b**) 110 r/min (**c**) 120 r/min

Figure 25. Images of basalt cores during drilling at three rotational speeds.

The underlying mechanism of this phenomenon is closely related to the high hardness and poor drillability of basalt rock. The drill bit inevitably generates radial runout during rotation, which applies continuous radial loading to the rock core. Combined with the foregoing single-depth test results, lower rotational speed prolongs the rock-breaking duration within basalt. Accordingly, the core endures prolonged and repeated radial excitation, which readily initiates internal microcracks and structural damage. After the bit fully penetrates the rock, the constraint from the borehole wall effectively suppresses bit

radial runout and weakens the radial load acting on the core. At this stage, core integrity is mainly dominated by frictional interaction with the inner wall of the coring bit. Such interfacial friction promotes the propagation of internal microcracks, eventually triggering brittle fracture of the rock core. Moreover, after bit penetration into the basalt formation, a lower rotational speed corresponds to a larger sliding friction coefficient between the core and the coring tube wall. This increases interfacial friction and exacerbates the non-uniform stress distribution inside the core. Consequently, coring at a lower rotational speed makes the rock core more vulnerable to fracture.

5.2.3. Drilling Force Analysis

Figure 26 presents the variation in maximum drilling force across successive drilling runs under three rotational speeds.

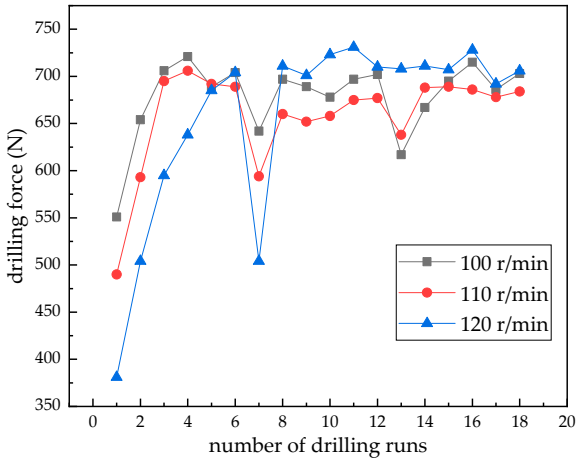


Figure 26. Drilling force comparison.

As illustrated in the figure, the maximum drilling force at all three rotational speeds rises from the first to the fourth drilling run with an increasing number of runs. Additionally, the maximum drilling force exhibits a negative correlation with rotational speed in this stage: the magnitude is the highest at 100 r/min and the lowest at 120 r/min.

From the fifth drilling run onward, the maximum drilling force fluctuates within a stable range as drilling continues. Overall, the maximum drilling force reaches the highest level at 120 r/min and the lowest at 110 r/min, while the most pronounced fluctuation occurs at 100 r/min. Between the eighth and 18th drilling runs, the average maximum drilling force at 100 r/min, 110 r/min, and 120 r/min is 686 N, 671.36 N, and 711.64 N, respectively. The results reveal that a higher rotational speed initially reduces the maximum drilling force during coring. Nevertheless, as bit wear accumulates progressively, the maximum drilling force increases gradually and eventually stabilizes with fluctuations around 700 N for all three rotational speeds.

In the initial drilling stage, the drill bit remains relatively sharp. Rock breaking is dominated by shear fragmentation supplemented by compressive fragmentation, which leads to a low demand for maximum drilling force. As the drill bit gradually wears, its shear rock-breaking capacity deteriorates continuously, thereby raising the required maximum drilling force. With further accumulation of drilling runs, bit wear is continuously aggravated. Once the drill bit becomes fully blunted, the rock-breaking mechanism is dominated by compressive fragmentation. The cutting resistance tends to stabilize correspondingly, and the maximum drilling force converges to approximately 700 N.

In summary, the maximum drilling force at 110 r/min remains at a relatively low level throughout the tests. After the drill bit wears to a steady state, the force variation exhibits

minor fluctuations and good stability, implying superior durability of the drill bit at this optimal rotational speed.

5.2.4. Drilling Torque Analysis

Figure 27 shows the variation in maximum drilling torque during each drilling run at three rotational speeds.

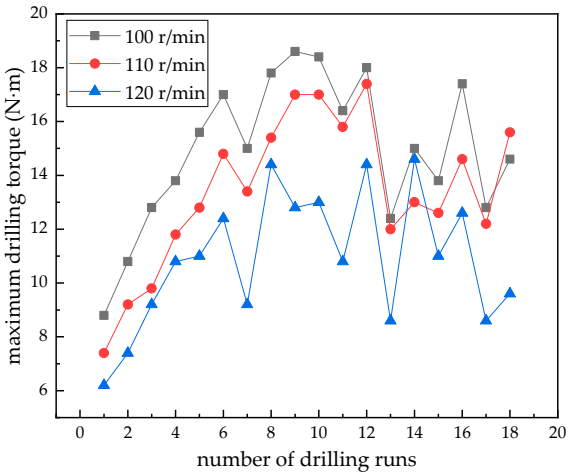


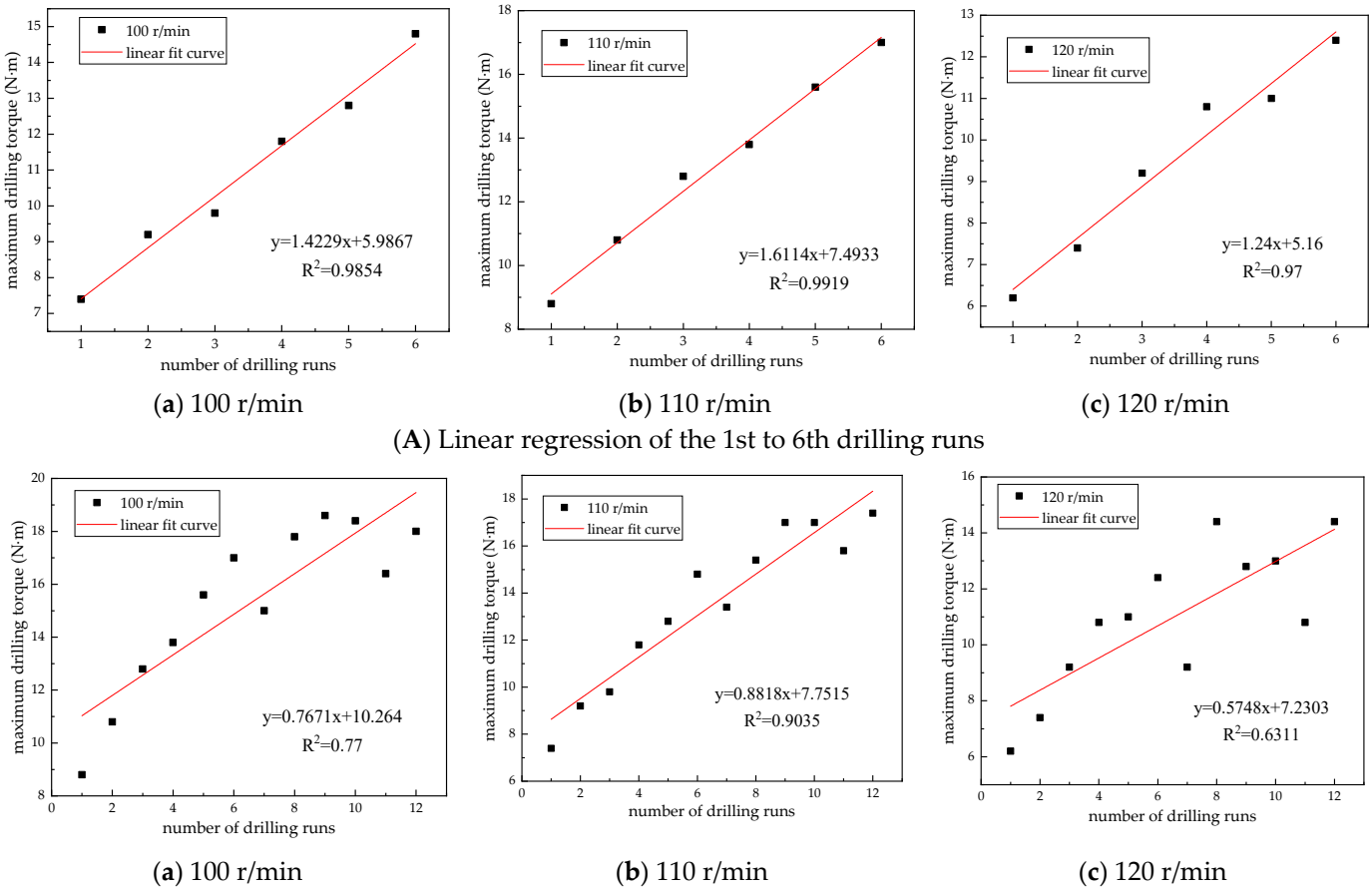
Figure 27. Drilling torque comparison.

As shown in the figure, at identical drilling runs, the maximum torque is the lowest at 120 r/min and the highest at 100 r/min. For all three rotational speeds, the maximum drilling torque increases with the number of drilling runs. After reaching a peak value, the maximum torque gradually declines and undergoes substantial fluctuations as drilling proceeds. The peak torque values for 100 r/min, 110 r/min and 120 r/min occur at the ninth run (18.6 N·m), the 12th run (17.4 N·m) and the eighth run (14.4 N·m), respectively.

When the drill bit remains sharp, shear-dominated rock breaking produces low cutting resistance and correspondingly low torque. As bit wear accumulates, the shear rock-breaking capability deteriorates continuously, resulting in increased cutting resistance and a gradual rise in drilling torque. Once the drill bit becomes fully blunted, cutting resistance tends to stabilize, and the rock-breaking mechanism shifts to compressive fragmentation dominance. Basalt is a typical highly brittle rock, and its compressive fracture behavior exhibits prominent randomness and instability. Meanwhile, accumulated drilling cuttings cause significant variations in the friction coefficient between the drill bit and the borehole wall, further inducing obvious fluctuations in maximum drilling torque. In addition, as drilling depth increases, the rock core inside the coring chamber grows longer, and the interfacial friction between the core and the inner wall of the coring bit further exacerbates torque fluctuation.

Consequently, the maximum drilling torque at 110 r/min maintains a rising trend over the longest duration of drilling runs. This phenomenon indicates that the drill bit retains its effective drilling performance for a longer service life at this optimal rotational speed.

To further clarify the evolutionary characteristics of maximum drilling torque, linear regression analysis was performed between the maximum torque and the number of drilling runs for the three rotational speeds, covering two stages: the 1st–6th runs and the 1st–12th runs. The corresponding linear regression results are presented in Figure 28.



(**a**) 100 r/min (**b**) 110 r/min (**c**) 120 r/min

(**A**) Linear regression of the 1st to 6th drilling runs

(**a**) 100 r/min (**b**) 110 r/min (**c**) 120 r/min

(**B**) Linear regression of the 1st to 12th drilling runs

Figure 28. Linear regression of maximum torque at different rotational speeds during drilling.

As illustrated in Figure 28, within the 1st–6th drilling runs, the maximum drilling torque exhibits a strong positive linear correlation with the number of runs at all three rotational speeds. The coefficients of determination R^2 are 0.9854, 0.9919 and 0.97 for 100 r/min, 110 r/min and 120 r/min, respectively. For the extended stage of the 1st–12th runs, the maximum torque at 110 r/min still maintains a good positive linear correlation with the drilling number, with R^2 = 0.9035. In contrast, the linear correlation weakens obviously at 100 r/min and 120 r/min, with R^2 declining to 0.77 and 0.6311, respectively. This indicates that the maximum torque at 100 r/min and 120 r/min begins to fluctuate significantly from the seventh to the 12th drilling run.

The regression results further confirm that a higher rotational speed yields a lower maximum torque during coring. At the initial drilling stage, the maximum torque increases linearly with the accumulation of drilling runs. As bit wear gradually accumulates to a critical level, the rock-breaking performance of the drill bit deteriorates, accompanied by a decline in maximum torque and severe torque fluctuation. Combined with the variation law of maximum drilling torque, the positive linear correlation between torque and drilling runs can be maintained for the longest duration at 110 r/min. It further verifies that the drill bit can sustain high-efficiency drilling for a longer service period at 110 r/min compared with the cases at 100 r/min and 120 r/min.

5.2.5. Drilling Temperature Rise Analysis

Figure 29 depicts the variation in maximum drill bit temperature across successive drilling passes at the three rotational speeds.

The results indicate that, at the same drilling run, the maximum bit temperature rises with increasing rotational speed, presenting the highest value at 120 r/min and the lowest at 100 r/min. The peak measured temperatures are 293.6 °C, 336.2 °C and 372.4 °C for 100 r/min, 110 r/min and 120 r/min, respectively. For all three rotational speeds, the maximum drill bit temperature shows an overall increasing trend as the number of drilling passes increases. A sharp temperature rise is observed from the first to the sixth pass, whereas the growth rate decreases markedly from the seventh to the 18th pass. Moreover, the bit temperature gradually tends to stabilize during the 13th to 18th drilling passes.

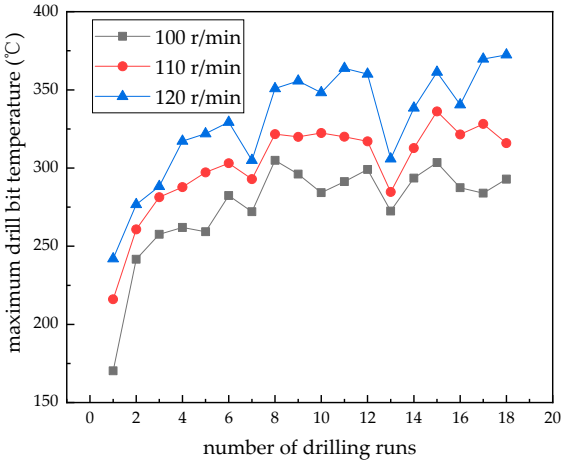
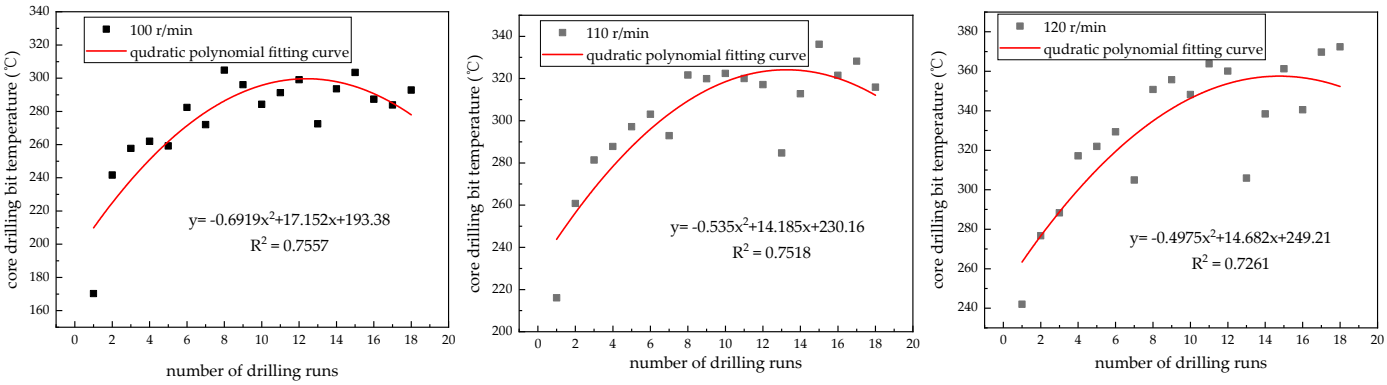


Figure 29. Temperature variation in core drill bit with number of drilling runs.

Overall, as presented in Figure 30, the drill bit temperature at the three rotational speeds follows a quadratic polynomial relationship with the number of drilling passes. The coefficients of determination R^2 for the quadratic regression of maximum bit temperature are 0.7557, 0.7518 and 0.7261 at 100 r/min, 110 r/min and 120 r/min, respectively.



(**a**) 100 r/min (**b**) 110 r/min (**c**) 120 r/min

Figure 30. Quadratic polynomial fitting of core drill bit temperature.

The regression results reveal that bit temperature rises rapidly with the increase in drilling runs at the initial stage, and a higher rotational speed corresponds to a higher bit temperature. As drilling runs continue to accumulate, progressive bit wear deteriorates the cutting performance, which weakens the temperature growth rate and eventually makes the temperature fluctuate within a relatively stable range. This behavior is mainly governed by the cutting and frictional heat generated during basalt drilling, which dominates the continuous temperature rise. Nevertheless, the peak temperature does not exceed the thermal stability limit of cemented carbide [31]. A higher rotational speed induces greater

heat generation per unit time. With ongoing bit wear, the heat generated in each drilling pass gradually tends to be steady. Meanwhile, the initial bit temperature accumulates continuously under repeated cyclic drilling, resulting in a gradual increase in the peak temperature at the end of each pass.

Furthermore, the elevated bit temperature enlarges the thermal gradient between the drill bit and the surrounding environment, thereby accelerating convective and radiative heat dissipation. In addition, bit wear increases the contact area between the drill bit and basalt borehole wall, further enhancing heat exchange and dissipation. Under the coupled influence of heat accumulation, heat dissipation and progressive bit wear, the maximum drill bit temperature gradually reaches a stable state in the late drilling stage.

6. Conclusions

In this study, dedicated to the Mars Sample Return mission, a cemented carbide coring drill bit was structurally designed and optimized. Drilling and wear experiments were performed on stimulant Martian soil and basalt, and the drilling performance, wear evolution, and optimal operating parameters in Martian soil–rock composite strata were systematically examined. The main conclusions are as follows:

(1) The proposed coring sampler features a reasonable structure and meets coring requirements for Martian soil–rock composite strata. The bit substrate is made of 40CrNiMoA alloy steel, equipped with YG6X cemented carbide cutting edges. Its key geometric parameters are specified as follows: cone angle of 130°, rake angle of 0°, clearance angle of 15°, four cutting edges, bottom protrusion of 2 mm, and outer protrusion of 2 mm.

(2) During coring in stimulant Martian soil, the feed to rotation ratio, relative density, and median particle size exert significant influences on sampling efficiency. Both drilling efficiency and acquired sample mass increase with a rising feed-to-rotation ratio. Sample mass is positively correlated with soil density and increases with decreasing median particle size; notably, it is considerably enhanced by introducing large particles into fine-grained soil.

(3) For basalt coring, a higher rotational speed accelerates bit wear and temperature elevation. At 120 r/min, the flank wear, mass loss, and peak temperature (372.4 °C) all reach their maximum values. The drill bit penetrates basalt mainly through compressive grinding, generating fine powdery cuttings. The dominant wear mechanism is abrasive wear, and the wear mass presents an approximately linear increase with drilling depth.

(4) In basalt coring, a low rotational speed tends to induce core fracture. Although 120 r/min yields the highest core recovery rate, it causes severe bit wear and excessive temperature rise. By contrast, 110 r/min achieves an optimal comprehensive balance between core integrity and bit service life. At this rotational speed, the attenuation of drilling depth is the slowest, the drilling force and torque remain stable, and the drill bit maintains efficient cutting performance over long-term operation.

The developed cemented carbide coring bit possesses a simple structural design, favorable machinability, and strong adaptability to Martian soil–rock composite strata. Under simulated Martian environmental conditions, it delivers high drilling efficiency, qualified sampling quality, and outstanding wear resistance. The findings provide solid experimental support and valuable engineering guidance for the structural development and parameter optimization of planetary drilling and coring systems for Mars exploration.

Author Contributions: Conceptualization, W.X. and Y.T.; methodology, Y.L. (Yuyang Liu) and Y.S.; test sample preparation, J.Z. (Jiahang Zhang); validation, J.J. and W.W.; investigation, W.G.; data curation, J.Z. (Jialin Zhang); writing—original draft preparation, W.Z.; project administration, Y.L. (Yafang Liu). All authors have read and agreed to the published version of the manuscript.

Funding: This research was funded by Fundamental Research Funds in Universities of Heilongjiang Province (2024KYYWF0997), National Key Research and Development Program Project (2022YFA1204604), Key Research and Development Program of Heilongjiang Province (GY2024Zb0058).

Data Availability Statement: The raw data generated in this study cannot be publicly released owing to institutional confidentiality restrictions. Data are available from the corresponding author on reasonable request with official approval.

Conflicts of Interest: Author Wenhui Guo was employed by the company Guizhou Aerospace Qunjian Precision Machinery Co., Ltd. The remaining authors declare that the research was conducted in the absence of any commercial or financial relationships that could be construed as a potential conflict of interest.

References

1. Li, B.; Zhang, C.; Sheng, C.; Fan, J.; Liu, D. Design and Experiment of Deployment Mechanism for Mars Subsurface Radar. *Chin. Space Sci. Technol.* **2023**, *43*, 87–93. [CrossRef]
2. Yang, M.; Zheng, Y.; Ni, Y.; Huang, X.; Zhang, Z.; Xing, Z. Progress and Prospect in Planetary Exploration of Solar System. *Chin. Space Sci. Technol.* **2023**, *43*, 1–12.
3. Lyu, J.; Li, Q.; Hu, D.; Luo, H.; Zou, X. Mechanical Model for Lunar Surface Sampling Based on Modular Theory. *Chin. Space Sci. Technol.* **2023**, *43*, 63–72. [CrossRef]
4. Yuan, Z.; Mu, R.; Zhao, H.; Wang, K. Predictive Model of a Mole-Type Burrowing Robot for Lunar Subsurface Exploration. *Aerospace* **2023**, *10*, 190. [CrossRef]
5. Van Winnendael, M.; Baglioni, P.; Vago, J. Development of the ESA ExoMars Rover. In *Proceedings of the 8th International Symposium on Artificial Intelligence, Robotics and Automation in Spacee (iSAIRAS 2005), Munich, Germany, 5–8 September 2005*; ESA: Noordwijk, The Netherlands, 2005; pp. 15–22.
6. Di Lizia, P.; Bernelli-Zazzera, F.; Ercoli-Finzi, A.; Mottola, S.; Fantinati, C.; Remetean, E.; Dolives, B. Planning and Implementation of the On-comet Operations of the Instrument SD2 onboard the Lander Philae of Rosetta Mission. *Acta Astronaut.* **2016**, *125*, 183–195. [CrossRef]
7. Bar-Cohen, Y.; Zacny, K. *Drilling in Extreme Environments: Penetration and Sampling on Earth and other Planets*; WILEY-VCH Verlag GmbH & Co. KGaA: Weinheim, Germany, 2009; pp. 393–399.
8. Anttila, M. Concept Evalution of MARS Drilling and Sampling Instrument. Ph.D. Thesis, Helsinki University of Technology, Espoo, Finland, 2005; pp. 62–69.
9. Kerry, K.; Mircea, B.; Nicolas, H.; Lori, S.; Phillip, W. Development and Testing of a Rotary Percussive Sample Acquisition Tool. In Proceedings of the IEEE Aerospace Conference, Big Sky, MT, USA, 3–10 March 2012; pp. 1–9. [CrossRef]
10. Zacny, K.; Cooper, G. Coring Basalt under Mars Low Pressure Conditions. *Mars* **2007**, *3*, 1–11. [CrossRef]
11. Zacny, K.; Paulsen, G.; Szczesiak, M. Challenges and Methods of Drilling on the Moon and Mars. In Proceedings of the 2011 Aerospace Conference, Big Sky, MT, USA, 5–12 March 2011; pp. 1–9. [CrossRef]
12. Anderson, R.C.; Jandura, L.; Okon, A.B.; Sunshine, D.; Roumeliotis, C.; Beegle, L.W.; Hurowitz, J.; Kennedy, B.; Limonadi, D.; McCloskey, S.; et al. Collecting samples in Gale Crater, Mars; an Overview of the Mars Science Laboratory Sample Acquisition, Sample Processing and Handling System. *Space Sci. Rev.* **2012**, *170*, 57–75. [CrossRef]
13. Spohn, T.; Hudson, T.L.; Marteau, E.; Golombek, M.; Grott, M.; Wippermann, T.; Ali, K.S.; Schmelzbach, C.; Kedar, S.; Hurst, K.; et al. The InSight HP^3 Penetrator (Mole) on Mars: Soil Properties Derived from the Penetration Attempts and Related Activities. *Space Sci. Rev.* **2022**, *218*, 72. [CrossRef]
14. Spohn, T.; Hudson, T.L.; Witte, L.; Wippermann, T.; Wisniewski, L.; Kedziora, B.; Vrettos, C.; Lorenz, R.D.; Golombek, M.; Lichtenheldt, R.; et al. The InSight-HP^3 Mole on Mars: Lessons Learned from Attempts to Penetrate to Depth in the Martian Soil. *Adv. Space Res.* **2022**, *69*, 3140–3163. [CrossRef]
15. Brasser, R.; Mojzsis, S.J.; Matsumura, S.; Ida, S. The cool and distant formation of Mars. *Earth Planet. Sci. Lett.* **2017**, *468*, 85–93. [CrossRef]
16. Bridges, J.C.; Catling, D.C.; Saxton, J.M.; Swindle, T.D.; Lyon, I.C.; Grady, M.M. Alteration Assemblages in Martian Meteorites: Implications for Near-surface Processes. *Space Sci. Rev.* **2001**, *96*, 365–392. [CrossRef]
17. Banham, S.G.; Gupta, S.; Rubin, D.M.; Edgett, K.S.; Barnes, R.; Van Beek, J.; Watkins, J.A.; Edgar, L.A.; Fedo, C.M.; Williams, R.M.; et al. A Rock Record of Complex Aeolian Dedforms in A Hesperian Desert Landscape: The Stimson Formation as Exposed in the Murray Buttes, Gale Crater, Mars. *J. Geophys. Res. Planets* **2021**, *126*, e2020JE006554. [CrossRef]
18. Golombek, M.; Rapp, D. Size-frequency Sistributions of Rocks on Mars and Earth Analog Sites: Implications for Future Landed Missions. *J. Geophys. Res.* **1997**, *102*, 4117–4130. [CrossRef]

19. Gorevan, S.P.; Myrick, T.; Davis, K.; Chau, J.J.; Bartlett, P.; Mukherjee, S.; Anderson, R.; Squyres, S.W.; Arvidson, R.E.; Madsen, M.B.; et al. Rock Abrasion Tool: Mars Exploration Rover Mission. *J. Geophys. Res. Planets* **2003**, *108*, 8068. [CrossRef]
20. Moeller, R.C.; Jandura, L.; Rosette, K.; Robinson, M.; Samuels, J.; Silverman, M.; Brown, K.; Duffy, E.; Yazzie, A.; Jens, E.; et al. The Sampling and Caching Subsystem (SCS) for the Scientific Exploration of Jezero Crater by the Mars 2020 Perseverance Rover. *Space Sci. Rev.* **2021**, *217*, 5. [CrossRef]
21. Liu, Y.; Zhang, L.; Tian, Y.; Zhang, W.; Tang, J.; Zhang, J.; Duan, Z.; Ji, J. Design and Experimental Study of a Drilling Tool for Mars Rock Sampling. *Aerospace* **2024**, *11*, 272. [CrossRef]
22. Herd, C.D.K.; Bosak, T.; Hausrath, E.M.; Hickman-Lewis, K.; Mayhew, L.E.; Shuster, D.L.; Siljeström, S.; Simon, J.I.; Weiss, B.P.; Wadhwa, M.; et al. Sampling Mars: Geologic Context and Preliminary Characterization of Samples Collected by the NASA Mars 2020 Perseverance Rover Mission. *Proc. Natl. Acad. Sci. USA* **2025**, *2*, 122. [CrossRef]
23. Ouyang, Z.Y.; Xiao, F.G. Major Scientific Issues Involved in Mars Exploration. *Spacecr. Environ. Eng.* **2012**, *28*, 205–217.
24. Herkenhoff, K.E.; Golombek, M.P.; Guinness, E.A.; Johnson, J.B.; Kusack, A.; Gorevan, S.; Richter, L.; Sullivan, R.J. Chapter 20: In Situ Observations of the Physical Properties of the Martian Surface. In *The Martian Surface: Composition, Mineralogy, and Physical Properties*; Bell, J., Ed.; Cambridge University Press: Cambridge, UK, 2008.
25. Demir, Z. An Experimental Investigation of the Effects of Point Angle o the High Speed Steel Drills Performance in Drilling. *Meas. Control* **2018**, *51*, 002029401879785. [CrossRef]
26. Peng, X.; Zeng, T.; Yin, Z.; Zhao, Z.; Li, L. Experimental Study on Drilling Basalt with Small Diameter Drilling Tools. *Adv. Space Res.* **2019**, *64*, 1117–1187. [CrossRef]
27. Xue, L. Engineering of Martian Soil Simulant and in Situ Identification of Terrain Parameter for Planetary Rovers. Ph.D. Thesis, Jilin University, Changchun, China, June 2017.
28. Chen, C.B. Load Characteristics of Drilling and Coring in Lunar Regolith Simulant and Drilling Control Investigation. Ph.D. Thesis, Harbin Institute of Technology, Harbin, China, March 2017.
29. Blake, D.F.; Morris, R.V.; Kocurek, G.; Morrison, S.M.; Downs, R.T.; Bish, D.; Ming, D.W.; Edgett, K.S.; Rubin, D.; Goetz, W.; et al. Curiosity at Gale Crater, Mars: Characterization and Analysis of the Rocknest Sand Shadow. *Science* **2013**, *341*, 6153. [CrossRef] [PubMed]
30. Qi, S.; Li, L.; Hou, X.; Qiao, S.; Ma, X.; Lu, X.; Cong, J.; Hao, R.; Zhang, C.; Li, J.; et al. Strongly cohesive lunar soil identified at the chang'e-6 landing site. *Nat. Astron.* **2025**, *10*, 214–223. [CrossRef]
31. Dai, Z.Y.; Yu, Y.; Liu, Y.L.; Fang, G.K.; Qiao, Z.H. Tribological Properties of Ultrafine-grained WC-6Co Cemented Carbide over A Wide Temperature Range: Influence of Titanium Alloy and Bearing Steel Counterparts. *Foundry Technol.* **2025**, *46*, 680–688. [CrossRef]

Disclaimer/Publisher's Note: The statements, opinions and data contained in all publications are solely those of the individual author(s) and contributor(s) and not of MDPI and/or the editor(s). MDPI and/or the editor(s) disclaim responsibility for any injury to people or property resulting from any ideas, methods, instructions or products referred to in the content.